This non-peer reviewed preprint has been submitted for publication in a Geological Society of London Special Publication. Subsequent versions of the manuscript may be somewhat different.

The effects of stress gradients on faulting and dike emplacement, with applications to Santorini and Iceland

Agust Gudmundsson

Department of Earth Sciences, Royal Holloway University of London, Queen's Building, Egham TW20 0EX, UK (rock.fractures@googlemail.com, Agust.Gudmundsson@rhul.ac.uk)

Abstract

All tectonic rock fractures develop in response to local stresses. The stress conditions for fracture formation has been analysed theoretically and experimentally and used to explain fracture patterns and activity in the field. How the local stresses themselves are generated, and then modified through fracture development, has received less attention. Here I show how local stress fields arise because of stress concentrations around rocks with elastic properties that differ from those of the surrounding rocks. Large-scale stress raisers include cavities (such as magma chambers) and elastic inclusions (such as fault zones). One main mechanical effect of tectonic fracture formation and development is to lower the raised stresses and thereby reduce the local stress gradient. Using dikes in Santorini (Greece) as an example of fluid-driven extension fractures, I show how their magmatic overpressure during emplacement tends to bring the local stresses closer to isotropic. Similarly, using normal, reverse, and strike-slip faults in Iceland as examples, I show how their formation and subsequent slips bring the local stress field closer to isotropic. Based on these examples, and a general theoretical framework, it is concluded that all tectonic fracture formation tends to bring the state of stress towards isotropic, thereby reducing the local stress gradients.

Why do rock fractures develop in the earth's crust? What is the basic reason for their formation? More generally, what are the mechanical conditions for brittle deformation in the earth's crust? Brittle deformation in the earth's crust occurs everywhere, but on a large scale it is most marked at and close to plate boundaries such as mid-ocean ridges, transform faults, and subduction zones. The deformation at these boundaries is characterised by rock-fracture formation and development. The fractures are the primary control on many of the earth's physical processes inside and outside plate boundaries, including crustal-fluid transport, tectonic earthquakes, and volcanic eruptions.

Mechanically there are two types of rock fractures: extension fractures and shear fractures. Extension fractures form in response to normal stresses, whereas shear fractures form in

response to shear stresses. Extension fractures are further divided into two main classes: tension fractures and fluid-driven fractures – the latter are also named hydrofractures (Gudmundsson, 2011). Large-scale tectonic tension fractures are common at mid-ocean ridges and other divergent plate boundaries and areas undergoing extension. They rarely reach the depth of a kilometre, and are mostly in the depth range of up to a few hundred metres. Fluid-driven fractures, by contrast, can form at any depth in the brittle crust, and include most joints, as well as dikes, inclined sheets, and sills (Tibaldi, 2015; Gudmundsson, 2020). Shear fractures comprise all faults and include also some joints. Faults and joints are very common at plate boundaries and are also found everywhere in the brittle part of the earth's crust. At deeper levels in the crust, there is ductile deformation, but in this paper the focus is on brittle deformation.

So coming back to the initial question: what are the conditions for rock fractures to form? And once formed what mechanical changes do the fractures bring to the crustal segment or rock layer/unit within which they form? Here I suggest that rock fractures form primarily in response to stress gradients, namely differences in stress magnitudes between locations within a given volume of a crustal segment or a rock body. Furthermore, I propose that one main mechanical effect of fracture formation is the reduction of an associated stress gradient. Thus, on this view, brittle deformation occurs primarily as a means of minimising stress gradients in the crust.

The aim of this paper is, first, to explain how stress gradients in the brittle crust arise and, second, how they are reduced (diminished) through brittle deformation. The focus is on the outcrop-scale structures, such as tectonic tension fractures, faults, and dikes that initiate and grow because of stress gradients and contribute to reducing those very same gradients. While the physical principles explored are completely general, the application is here to situations and structures observed in Santorini (Greece) and Iceland.

Gradients in nature

Before we discuss stress gradients, a brief overview of some common gradients in nature may be appropriate. Some of the common gradients that are related to geological processes may be briefly summarised as follows.

Geological gradients

One of the best known is the geothermal gradient. The general gradient indicates that the temperature in the earth increases with depth and reaches its maximum in the earth's core. But the gradients are also local, such as in volcanic areas and associated geothermal fields. For example, high-temperature fields in Iceland are defined so that the temperature at 1 km depth exceeds 200 °C (Saemundsson, 2009). The spontaneous (natural) flow of heat is from higher to lower temperature, that is, down the gradient. This follows from the second law of thermodynamics (which, itself, can be explained in terms of statistical physics and information theory (Sommerfeld, 1964; Sturge, 2003; Laurendeau, 2005; Desurvire, 2009)).

The direction of heat flow thus has the consequence of reducing any thermal gradient, and the geothermal gradient in particular.

Temperature gradients on different scales in the oceans and in the atmosphere supply the driving forces for ocean currents and wind (Andrews, 2010; Wells, 2011). The ocean currents, and the air masses, carry water/air from warm regions to cooler regions. So the flow is from warmer to cooler and thus down the temperature gradient.

Chemical concentration gradients are also common. Some occur in water, such as in polluted lakes, while others occur in the air. The latter are particularly common in urban areas where air pollution often results in health risks (Mohajeri et al., 2023). By diffusion and other means, the chemical concentration may become diluted. Again, the flow or diffusion is from higher to lower concentrations, so that the transport of the chemicals is down the gradient.

The hydraulic gradient constitutes a part of Darcy's law for fluid transport in porous media (Bear, 1988; Gudmundsson, 2011). This gradient controls the flow of groundwater and some other crustal fluids in porous solid rocks and in sediments and drives the fluids down the gradient from higher to lower potential energy.

Landscape or topographic gradients are very important in landscape evolution. These are controlled primarily by gravity in that erosional agents such as rivers and glaciers flow downhill and tend to level out the topography. The end stage in the evolution of landscape is a flat land with little or no topographic gradients, namely a peneplain. The material movement is then down the gradient.

Mathematical framework

All these gradients follow the same general mathematical principles, which may be briefly described as follows (Durrant, 1996; Marsden and Tromba, 2012). We start by introducing the vector differential operator del (nabla) which has the symbol ∇ and is defined as follows:

$$\nabla = \bar{i}\frac{\partial}{\partial x} + \bar{j}\frac{\partial}{\partial y} + \bar{k}\frac{\partial}{\partial z} = \left(\frac{\partial}{\partial x}, \frac{\partial}{\partial y}, \frac{\partial}{\partial z}\right) \tag{1}$$

where $\bar{i}$, $\bar{j}$ and $\bar{k}$ are unit vectors in the directions of the rectangular coordinate axes x, y and z , respectively, and the components of the operator are the partial derivatives, denoted by ∂. Consider a differentiable scalar field defined by the function $\phi(x, y, z)$ in a given region of space. Then the gradient of ϕ is defined as:

$$grad\phi = \nabla\phi = \bar{i}\frac{\partial\phi}{\partial x} + \bar{j}\frac{\partial\phi}{\partial y} + \bar{k}\frac{\partial\phi}{\partial z} = \left(\frac{\partial\phi}{\partial x}, \frac{\partial\phi}{\partial y}, \frac{\partial\phi}{\partial z}\right) \tag{2}$$

The gradient (Eq. 2) is a vector, which means that when the operator in Eq. (1) acts on a scalar field the operator generates a vector field (Eq. 2). Like any vector, the gradient has both magnitude and direction. The direction of the gradient $\nabla\phi$ (Eq. 2) is the direction in

which the function ϕ increases most rapidly. Conversely, the direction of the negative of the gradient, that is, of $-\nabla\phi$, is the direction in which the function ϕ decreases most rapidly – that is, down the gradient (which is the direction of the 'movement' or process in the geological gradients listed above). The magnitude of the gradient, $|\nabla\phi|$, is the rate of increase of ϕ in the direction of the gradient.

Topography is a simple way of visualising the gradient. For an active, regularly shaped stratovolcano, for example, the direction of $\nabla\phi$ is that of the steepest ascent to the top of the volcano. Similarly, the direction of $-\nabla\phi$ is the direction of the steepest descent from the top of the volcano. The magnitude of the gradient is then the slope in the direction of the steepest ascent.

In the stratovolcano analogy ϕ is a function of two variables (x and y being the map view) rather than three variables. In this case, we use $z = f(x, y)$ to plot the elevation above the base which for dry-land topography is usually taken as sea level. While we cannot show a drawing of a 3D scalar field - because all the three coordinate axes are already used to show the points (x, y, z) of the scalar field – we can use two-dimensional sections to present the three-dimensional field. More specifically, by using specific constant values of one of the variables, say z, then we define a section or surface, and by considering many different constant values of z we define many such surfaces which can be used to provide an image of the 3D scalar field.

Here we need to distinguish between a scalar field and a vector field. Any spatial distribution of a quantity defines a field. When the quantity is completely specified by a magnitude, that is, a single number (and a physical unit of measure), the quantity is a scalar. When a quantity needs, for its specification, a direction in space in addition to its magnitude, the quantity is a vector. The magnitude of the vector is a non-negative number, a scalar, and is sometimes referred to as the length of the vector. Examples of scalar quantities include pressure, temperature, mass as well as length, area and volume. Examples of vectors include force, velocity, and acceleration.

A scalar field occurs when a specific number, a magnitude, is associated with each point *(x, y, z)* in space. As indicated in Eq. (1), the scalar $\phi(x, y, z)$ corresponds to each of the points in the field and ϕ is referred to as a scalar function of position and a scalar field ϕ has been defined. Points of equal magnitude are commonly joined together by curves referred to as contour lines or contour curves. Thus contour lines join together points of equal magnitude. For example, contour lines join together points of equal pressure, such as isobars for atmospheric pressure, and points of equal elevation for topography. Other examples of scalar fields include temperature fields, and the distribution of mass in a body. In fluid transport, and in potential theory in general, curves that join together points of equal potential energy are referred to as equipotentials. If the scalar field is independent of time, it is referred to as a stationary or steady-state field.

A vector field occurs when a specific magnitude, a number, and direction, namely a vector **V**(*x, y, z*), is associated with each point *(x, y, z)* in space. The vector **V**(*x, y, z*) is referred to as a vector position function and a vector field **V** has then be defined. The field vectors are presented by arrows, with the tail end (beginning of the arrow) at the point where the field is specified, and the length of the arrow representing the size or magnitude of the vector at that point. Examples of vector fields include wind velocity and the gravitational field of a planet and a satellite. If the vector field is independent of time, it is referred to as a stationary or steady-state field. Here we consider only stationary vector (and scalar) fields.

A surface of a three-dimensional scalar field where the scalar has a constant value is referred to as either the contour surface or the level surface. In the stratovolcano analogy, these surfaces are elevation surfaces above sea level and on a map they are marked by contour lines. Thus the contour lines, or simply the contours, on a topographic map of a stratovolcano (or any other topographic feature) represent the intersections between the imaginary contour surfaces or level surfaces and the sloping surfaces or flanks of the stratovolcano.

The gradient has several further characteristics which may be summarised as follows. First, the gradient is perpendicular to level surfaces, such as equipotential surfaces or lines. For example, in a mountain the equipotential lines (and the corresponding surfaces) are the contours and the gradient is thus perpendicular to the contours (contour lines). In areas of stress concentration, the equipotential lines are the contours showing stresses of equal magnitude, as discussed in detail later in the paper. Second, the gradient is a generalisation to three-dimensions of the derivative. The derivative is zero where the curve of a function is changing from convex to concave, or vice versa. Similarly, the gradient is zero, $\nabla\phi = 0$ (Eq. 2), at stationary points of the function $\phi(x, y, z)$. The stationary points include a maximum (a summit or top – here of the stratovolcano), a saddle point (a pass), and a minimum (a valley floor). The gradient is also zero in a direction parallel with the equipotential surfaces and contour lines. Third, the magnitude of the gradient is large when the contours are close together and smaller when the contours are far apart.

In addition to the three mathematical points listed above, the following physical aspects of gradients should be mentioned. First, the ‘flow’ or transport is always from a higher concentration or energy to lower concentration or energy, that is, it is always down the gradient (as was mentioned for each of the geological gradients listed above). Second, because the flow or transport is from a higher to a lower concentration of energy the difference between the high and low tends to gradually diminish. In other words, the processes all result in the associated gradients being levelled out or, temporarily at least, destroyed.

The gradients of greatest importance for brittle deformation in the earth’s crust are the stress gradients. These gradients control fracture formation and, thereby, faulting and dike emplacement (and associated hazard), and to these we turn now..

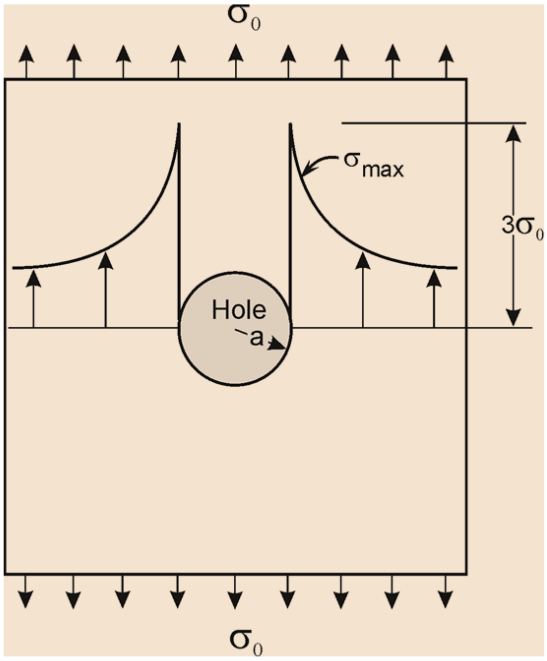

Fig. 1. Maximum tensile stress σ_{max} around a circular hole (of radius a) subject to tensile loading σ_0 occurs at the boundary of the hole and is 3-times the applied tensile stress. The stress falls off rapidly with distance from the hole.

Stress gradients

When there is significant difference in the stress magnitude between two or more sites that interact mechanically, then there is a stress gradient between the sites. For the gradient to exist, the sites must interact mechanically. This means that there is a mutual interaction between the stress fields of the sites. As we discuss below, sites of raised stress, of stress concentrations, are always local so that the high stresses are limited to a certain volume around the cause of the stress concentration.

The size of the mechanical interaction depends strongly on the size of the source of the stress concentration. Consider, as an example, the stress concentration around a circular hole subject to remote tensile stress. The maximum tensile stress due to the loading occurs at the boundary of the hole and is 3-times the applied tensile stress (Fig. 1). But the stress falls off rapidly with distance from the hole and soon becomes similar to the applied remote tensile stress. Here the stress gradient is thus due to the difference is tensile stress at the boundary of the hole, where it reaches a maximum, and the remote applied tensile stress.

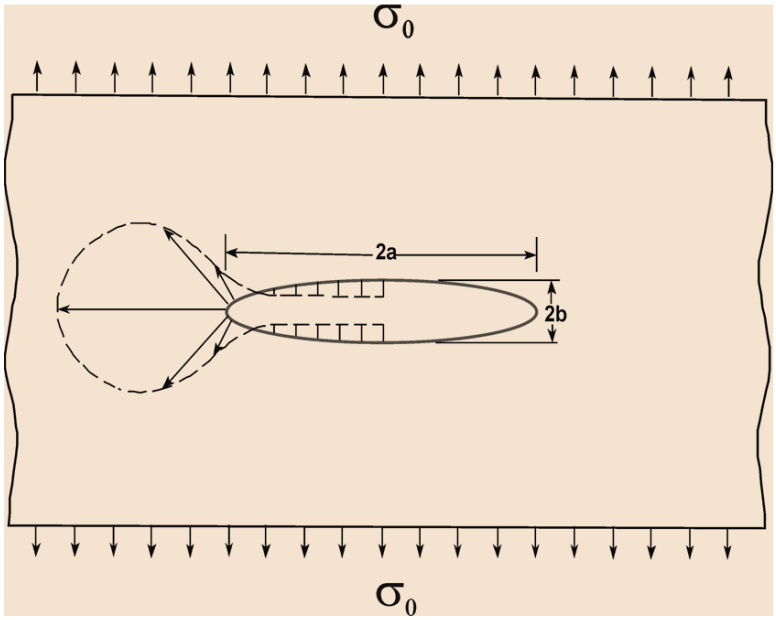

Fig. 2. Elliptical hole subject to remote tensile stress σ_0 in a direction perpendicular to the major axis, 2a, of the ellipse as the only loading. The maximum tensile stress concentration occurs at the lateral tips (as is indicated for the left tip), whereas there is compressive stress along part of the boundary of the ellipse, reaching its maximum compressive stress at the hole centre. Notice that for illustrative purposes tensile stress is here shown as positive, but in the present paper (and normally in geology) it is regarded as negative (modified from Boresi and Sidebottom, 1985).

That the maximum tensile stress at the boundary of a circular hole is 3-times the applied tensile stress follows from the general formula for stress concentration around an elliptical hole (Fig. 2), which is given by (Gudmundsson, 2011):

$$\sigma_{max} = \sigma_0\left(\frac{2a}{b}+1\right) \tag{3}$$

where σ_{max} is the maximum tensile stress at the boundary of an elliptical hole, σ_0 is the remote tensile stress loading in a direction perpendicular to the major (long) axis of the ellipse (*2a*), and *a* and *b* are the semi-major and semi-minor axes of the ellipse. The minus sign for the remote tensile stress is here omitted (as in Figs 1 and 2); but when quantified that stress is assigned a negative sign so that the resulting maximum stress is negative (since tensile stress is regarded as negative in geology). For a circular hole, the radius is constant, so that *a* = *b*, and Eq. (1) gives $\sigma_{max} = 3\sigma_0$ (Fig. 1).

While two-dimensional stress fields around holes are very useful, and often sufficient for understanding the salient features of specific geological processes and problems, geological structures are of course three-dimensional. A three-dimensional version of a hole is a cavity. A cavity that is filled with a fluid, a liquid (say water or magma) or gas raises or concentrates

Fig. 3. Basalt sill in East Iceland has the geometry of a flat ellipse (Fig. 2). When this sill was fluid it acted as a cavity that concentrated stresses mainly at its tips (one tip is indicated). After it solidified (as a sheet intrusion) it has acted as stiff (high Young's modulus) elastic inclusion – which also modifies the local stress in its vicinity. The farm houses provide a scale.

stress. In the crust many formerly liquid cavities eventually become solids. This applies to cavities initially filled with geothermal fluids or magma. A cavity filled with solid material with mechanical properties different from those of the surrounding solid material is in mechanics referred to as an elastic inclusion. Because their mechanical properties, particularly their Young's modulus, differ from that of the surrounding material, elastic inclusion also modify the stress field in their vicinity.

Stress gradients around magma chambers

Examples of fluid-filled cavities include active magma chambers, dikes, and sills (Fig. 3). Initially, dikes and sills are totally molten, and crustal magma chambers may for a while be totally molten, even if many shallow chambers are probably only partially molten for most of their lifetimes (Gudmundsson, 2020). Examples of solid-filled cavities, that is, of elastic inclusions, include small structures such as fossils and amygdales, larger structures such as dikes, sills (Fig. 3), and fault zones (Fig. 4), and very large structures such as fossil magma chambers, that is, plutons (Fig. 5).

While stress gradients around cavities can be analysed analytically (Gudmundsson, 2011), as soon as the geometries of the cavities become complex, and if the crustal segment hosting the cavity is heterogeneous, anisotropic (layered), or both, numerical modelling is the most appropriate method of stress-gradient analysis. The numerical modelling results presented here were made using the finite-element method (FEM) and the boundary-element method

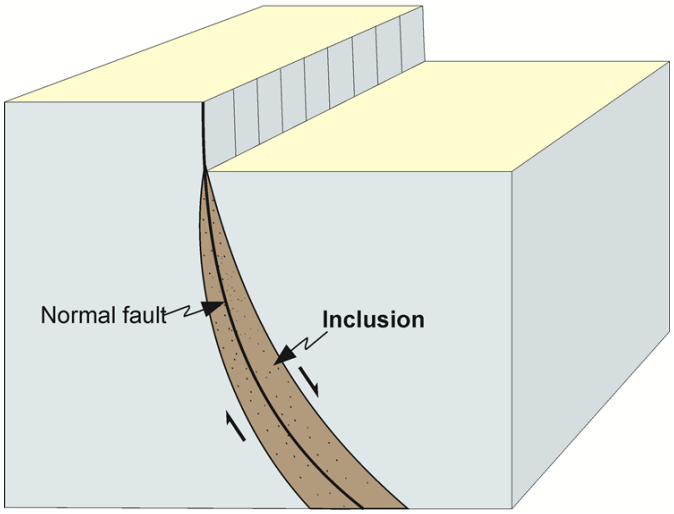

Fig. 4. Fault zone functions as an elastic inclusion. The fault rock, which is the core and the damage zone (shown together in brown colour), have elastic properties that differ from those of the host rock. Initially, while the fault is active, the fault rock is softer (lower Young's modulus) than the host rock, but later when the fault has be inactive for a long time the fault rock may become stiffer (e.g., due to compaction and secondary mineralisation) than the host rock. Both soft and stiff elastic inclusions modify the associated local stress field.

(BEM). These methods are described by Brebbia and Dominquez (1992), Deb (2006), and Logan (2016) and with application to rock-physics problems by Jing and Hudson (2002).

Consider first stress gradients around magma chambers. We start with the simplest model, namely that of a magma chamber with a circular vertical cross-section and located in a homogeneous, isotropic crustal segment with a Young's modulus (stiffness) of 40 GPa and a Poisson's ratio of 0.25 (Fig. 6). Here the only loading is magmatic excess pressure of 5 MPa inside the chamber. The inset indicates that the model is fastened (indicated by crosses), with the conditions of no displacement, in its lower parts. All subsequent numerical models in this paper are fastened in this way. The chamber is a shallow one and therefore comparatively close to the earth's free surface, which therefore has effect on the stress gradient.

The gradient is indicated by the contours of the maximum tensile (minimum compressive) principal stress, σ_3, around the chamber. These reach the maximum values of about 8 MPa at two localities on the upper margin of the chamber. From there, the tensile stress concentration gradually decreases away from the chamber and becomes essentially zero at a distance from the chamber margin that is similar to the chamber diameter.

Fig. 5. Fossil magma chamber, here a pluton (the Torres del Paine laccolith in Chile) mostly of granite, but underlain by a thick mafic pluton (Michel et al., 2008; cf. Gudmundsson, 2020). The granite part seen here is about 2 km thick and the (dark) roof and floor are seen. When fluid (some 12 million years ago), the chamber acted as a magma-filled cavity, but since its solidification as a stiff elastic inclusion. In both capacities the chamber modifies the surrounding local stresses (Photo: Evelyn Proimos/Flickr).

These results are entirely in harmony with analytical solutions for a circular hole close to a free surface, which is the model for a shallow chamber in Fig. 6. The circumferential stress at the boundary (the walls, roof, and floor) of the chamber σ_θ due to magmatic excess pressure p_e is given by (Savin1961; Gudmundsson, 2020):

$$\sigma_\theta = -p_e(1+2\tan^2\phi) \tag{4}$$

where p_e is the magmatic excess pressure inside the chamber. Here the angle ϕ is as defined in Fig. 7 and a minus sign is used to indicate that we are dealing with tensile stress. Because the upper part of the magma chamber is normally the one most likely to rupture and inject dikes or inclined sheets (Gudmundsson, 2006; Tibaldi, 2015), the focus is on that part. Inspection of Eq. (4) shows that the maximum value of σ_θ, denoted by σ_b, occurs at the points of maximum ϕ, which are where the line *AQ* is tangent to the boundary of the magma chamber, that is, at the points a_1 and a_2 where (Fig. 7). At these points, a_1 and a_2, the maximum tensile stresses become:

$$\sigma_b = -\frac{p_e(d^2+R_1^2)}{d^2-R_1^2} \tag{5}$$

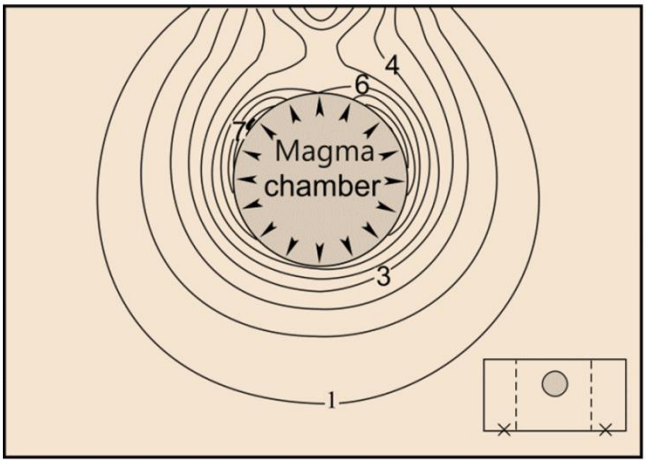

Fig. 6. Numerical model of tensile stress σ_3 around a magma chamber of circular vertical cross-section subject to magmatic excess pressure p_e of 5 MPa as the only loading (cf. Gudmundsson, 2011). The contours of σ_3 are in mega-pascals. The host rock is homogeneous and isotropic with a Young's modulus of 40 GPa and a Poisson's ratio of 0.25. The stress gradient shown is from a maximum of 8 MPa to 1 MPa.

where R_1 is the chamber radius and d is the depth to the centre of the chamber (Fig. 7). Comparison of Figs 6 and 7 shows that location of the maximum tensile stresses calculated through numerical and analytical methods coincide.

The numerical and analytical results also indicate that, for such a shallow chamber, there will be stress concentration at the surface above the chamber. This concentration is seen above the centre of the chamber in Fig. 6, and is in agreement with the following analytical solutions (Savin, 1961; Gudmundsson, 2020):

$$\sigma_t = -\frac{4p_e R_1^2}{d^2 - R_1^2} \tag{6}$$

and occurs at point *A* at the surface, right above the shallowest part, denoted by *B*, of the magma chamber (Fig. 7).

If, however, the magma chamber is far from the free surface of the associated volcanic system/field in relation to the size of the chamber, then the free surface has no effect on the local stress field around the chamber, and the stress decrease with distance from the boundary of the chamber follows a power function. When the chamber is modelled as a circular hole, a two-dimensional model, then the power-law variation in the radial compressive stress σ_r with radial distance *r* from the chamber margins (walls) is given by (Gudmundsson, 2020):

$$\sigma_r = p_e \left(\frac{R_1}{r} \right)^2 \tag{7}$$

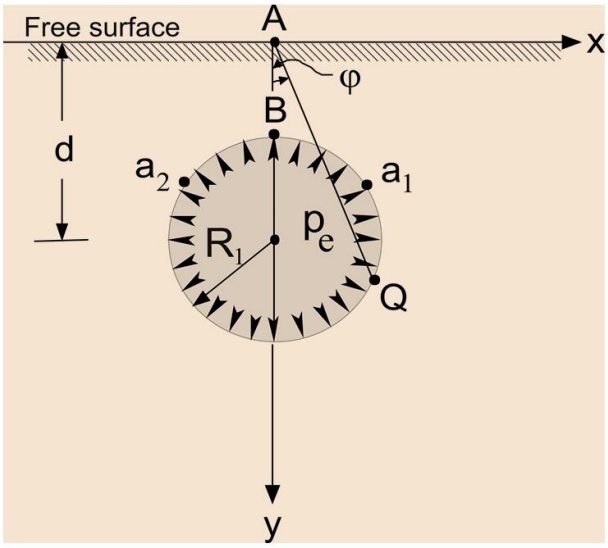

Fig. 7. Magma chamber with a circular vertical cross-section and a centre at depth *d* below the free surface (the surface of the volcano) is subject to magmatic excess pressure p_e as the only loading (cf. Gudmundsson, 2011). R_1 is the chamber radius, *A* is the point at the surface above the centre of the chamber, and *B* is the point on the boundary of the chamber closest to the surface. The maximum tensile stress occurs at the boundary of the chamber where the line *AQ* (which makes an angle φ to the y-axis) is a tangent to the boundary, namely at points a_1 and a_2.

and the power-law variation in the tensile stress σ_θ becomes:

$$\sigma_\theta = -p_e\left(\frac{R_1}{r}\right)^2 \tag{8}$$

Similarly, when the magma-chamber model is a spherical cavity whose radius is small in comparison with the chamber's distance below the free surface, the power-law variation in the radial compressive stress σ_r is:

$$\sigma_r = p_e\left(\frac{R_1}{r}\right)^3 \tag{9}$$

and the power-law variation in the two tensile principal stresses (which are equal because of spherical symmetry) σ_θ and σ_ϕ is:

$$\sigma_\theta = \sigma_\phi = -\frac{p_e}{2}\left(\frac{R_1}{r}\right)^3 \tag{10}$$

Here we use spherical polar coordinates (Fig. 8), namely r, θ, ϕ, where *r* is the radius vector (radial distance), θ is the angle between the radius vector *r* and a fixed axis *z*, and ϕ is the angle measured around this axis.

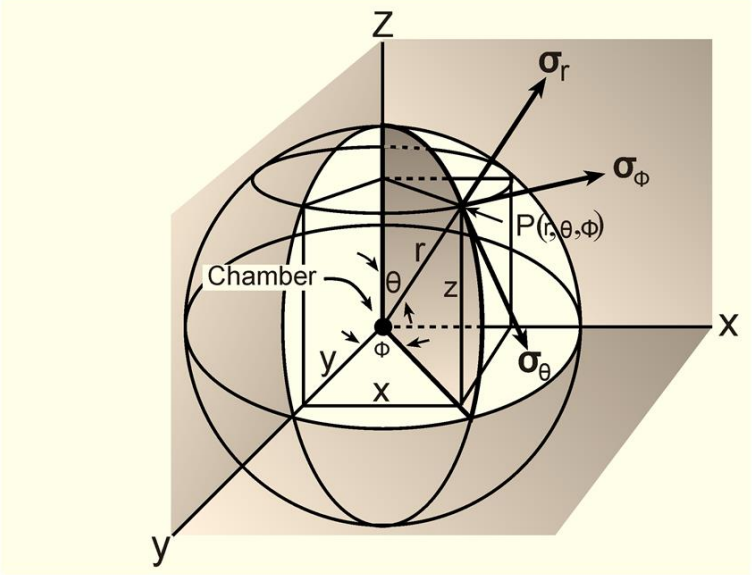

Fig. 8. Spherical coordinates for a spherical chamber (shown by a black dot in the centre) in a crustal segment. Indicated are the coordinates of a given point in the crust $P(r,\theta,\phi)$, the radial compressive stress σ_r, and the circumferential tensile stresses σ_θ and σ_ϕ associated with the magma chamber. The magmatic excess pressure *pe* is the only loading (cf. Gudmundsson, 2011).

To explore further how the stresses vary with distance from the margins of the chamber, we plot all the stresses as a function of distance from a chamber modelled as a circular hole (Fig. 9a) and modelled as a sphere (Fig. 9b). These plots are in accordance with Eqs. (7-10) and thus apply to chambers that are, in relation to the chamber size, far away from the free surface.

The stress gradient around the circular-hole chamber (Fig. 9a) shows a rapid decrease in all the stresses with increasing distance from the margin of the chamber. The decrease follows a power function. More specifically, the radial stress σ_r and the tensile stress σ_θ are both inversely proportional to r^2, that is, to the radial distance *r* squared so that the stresses diminish rapidly with increasing radial distance from the chamber (Fig. 9a). Thus, at a distance of one chamber diameter from the margin, that is, at $r = 2\ R_1$ (the origin of the *r* axis is in the centre of the chamber and the distance to its margin from the centre is $r = R_1$), both the stresses have reduced to ¼ of their value at the margin of the chamber (p_e) – in accordance with Eqs (7) and (8).

Similar, but steeper, stress gradients occur close to a magma chamber modelled as a sphere (Fig. 9b). The stresses are inversely proportional to r^3, that is, to the radial distance cubed (in the power of 3). It follows that the stresses diminish much more rapidly with distance from the margin or walls of a chamber modelled as a sphere than a chamber modelled as a circular hole. For example, at a distance of one chamber diameter from the margin, that is, at $r = 2\ R_1$, the radial (compressive) stress σ_r has diminished to 1/8 of its value at the margin of the chamber (p_e). The values of the tensile stresses σ_θ and σ_ϕ diminish at the same rate, but they

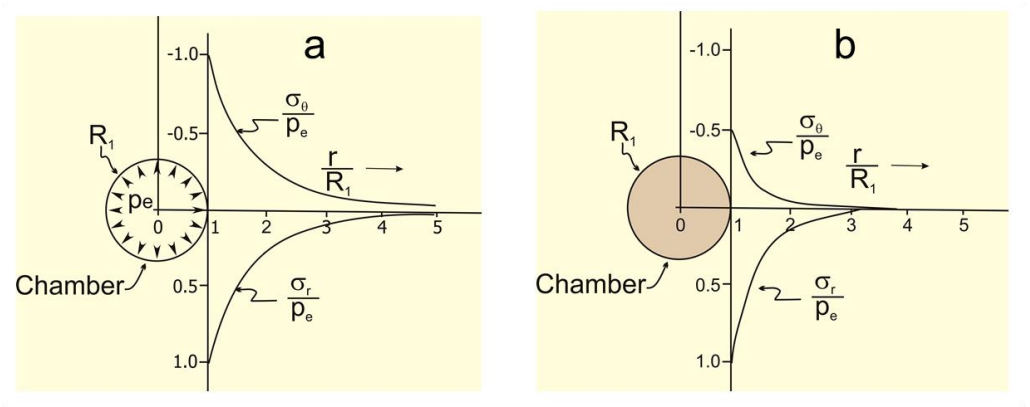

Fig. 9. Stress gradients around magma chambers modelled as a circular hole and a spherical cavity (cf. Gudmundsson, 2011). (a) The gradient of the radial σ_r and circumferential σ_θ stresses around a magma chamber modelled as a hole with a vertical circular cross-section of radius R_1 subject to excess magmatic pressure p_e as the only loading. The gradient magnitude decreases with the square of the distance r from the chamber. (b) The gradient of the radial σ_r and circumferential σ_θ stresses around a chamber modelled as a sphere. The chamber radius is R_1 and its only loading is excess magmatic pressure p_e. The gradient magnitude decreases with the cube of the distance r from the chamber.

start from a lower value at the margin of the chamber, namely at the value of $-0.5p_e$ rather than p_e.

All the above results (Figs 6-9) show that the stress gradient away from magma chambers is comparatively steep, that is, the stress magnitudes decrease rapidly with distance from the chamber margin. These are general results and apply to any magma chamber. But the details of the local stress gradients around a chamber depend on the chamber shape, the loading, and the mechanical properties of the host rock.

All volcanic zones, and all volcanoes, are composed of layers – lava flows, pyroclastic layers, intrusions – whose mechanical properties vary. In some basaltic edifices (shield volcanoes) all the rocks are basaltic and the layers may have similar mechanical properties, although contacts between layers add some anisotropy to the pile. But other basaltic edifices are partly formed in eruptions beneath glaciers, in which case basaltic breccia (hyaloclastite) units/layers form in-between the basaltic lava flows, resulting in edifices composed of layers with widely different mechanical properties. And all stratovolcanoes (composite volcanoes) are made of rock layers with widely different mechanical properties (Gudmundsson, 2020).

As an example of the effect of layering on the stress gradient, Fig. 10 shows how the tensile stress concentration varies around a magma chamber whose roof is composed of 30 layers on top of the unit hosting the chamber (whose Young's modulus is 40 GPa). The cross-sectional shape of the chamber is, again, circular and the only loading is an internal excess magmatic pressure (p_e) of 10 MPa. The layers have alternating Young's moduli of 1 GPa, as appropriate for some young pyroclastic or sedimentary layers, and 100 GPa, as suitable for some stiff lava flows and sill intrusions. The results show, first, that the highest tensile stresses (σ_3) at the margin of the chamber, about 20 MPa, occur at its upper margin, in a similar way to that of the chamber in Fig. 6. In the present model (Fig. 10), however, the maximum tensile stress is 2-times (20 MPa) the excess pressure (10 MPa), whereas in the earlier model (Fig. 6) the

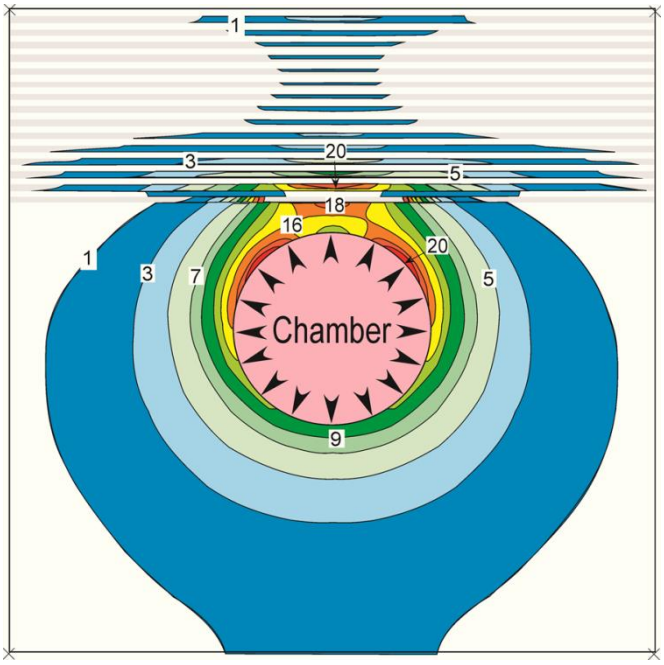

Fig. 10. Numerical model of the stress gradient around a magma chamber of circular vertical cross-section located in a crustal segment with 30 layers above the top of the chamber. The layers have alternating stiffness of 1 GPa (compliant) and 100 GPa (stiff). The only loading is magmatic excess pressure of 10 MPa in the chamber. The coloured contours indicate the maximum principal tensile stress σ_3 in mega-pascals. The results show that the magnitude of the stress gradient decreases smoothly away from the chamber within the host rock unit, but in an irregular (zig-zag) manner in the 30 layers above the chamber (cf. Gudmundsson, 2020).

maximum stress is only about 1.6-times (8 MPa) the excess pressure (5 MPa). This difference is primarily because of the compliant (1 GPa) layers above which encourage tensile stress concentration in the stiff units around and above the chamber.

The compliant layers also encourage tensile stress concentration in the high-Young's modulus, that is, stiff (100 GP) layers. The stiff layers show high stress concentrations whereas the compliant layers show little or no tensile stresses. This means that the tensile stress gradient upwards away from the magma chamber does not decrease in a smooth manner, as in Figs 6, 7, and 9, but in a zig-zag (or Christmas tree-like) manner. Such zig-zag gradients are the rule when the layering above the top of a cavity or hole - of any kind and subject to various types of loading – is such that compliant or soft layers alternate with stiff layers.

The chamber shape can also have strong effects on the geometry of stress gradients around magma chambers. Consider, for example, a sill-like (oblate ellipsoidal) magma chamber instead of a circular or spherical one. For a sill-like chamber in a homogeneous, isotropic crust and with internal excess pressure p_e as the only loading, the highest stresses are at the lateral ends of the chamber (Fig. 11). From there the tensile stress decreases smoothly away from the margin of the chamber. If the crustal segment hosting the chamber is layered, as it normally is, then there is still an overall decrease in the tensile stress away from the margin of the chamber (Fig. 12). However, the decrease is not along a smooth curve but rather with abrupt changes depending on the stiffness of the layers, particularly the stiffness contrast, similar to that observed around the circular chamber above (Fig. 10).

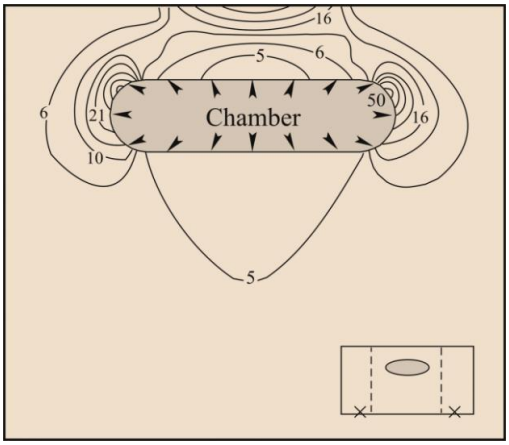

Fig. 11. Tensile stress gradients around a magma chamber modelled as a flat elliptical or sill-like hole in a homogeneous, isotropic crustal segment (cf. Gudmundsson, 2020). The contours of σ_3 are in mega-pascals. The only loading is magmatic excess pressure in the chamber of 5 MPa. The crustal segment has a Young's modulus of 40 GPa and a Poisson's ratio of 0.25. The gradient shown here is from 50 MPa at the lateral tips to 5 MPa, but it decreases to lower values at greater distances from the tips.

The type of loading has also great effects on the stress gradients. For example, when a circular magma chamber at a comparatively shallow depth in a homogeneous, isotropic crustal segment is subject to horizontal tension as the only loading, the resulting stress gradients are as given in Fig. 13. These gradients are very different from those of the same magma chamber geometry and location but subject to internal excess pressure as the only loading (Fig. 6). Similarly, when there is doming (small rise) of the crustal segment hosting a sill-like magma chamber the resulting stress gradients are different from those generated when the only loading is internal excess pressure (Figs 11 and 12). This difference in gradient applies both to doming of a sill-like chamber in a homogeneous, isotropic crustal segment (Fig. 14) as well as to doming of such a chamber in a layered crustal segment (Fig. 15). In both cases there is a shift in the location of the main stress concentration, when compared with the stress concentration with excess pressure as the only loading.

Stress gradients around elastic inclusions

Solidified intrusions, including sheet-like ones such as dikes, inclined sheets, and sills (Tibaldi, 2015; Gudmundsson, 2020) as well as fossil magma chambers (plutons), and some active volcanoes can act as elastic inclusions. In fact, any rock body that is located within a hosting crustal segment with different elastic properties acts as an elastic inclusion. Thus, fault zones also act as elastic inclusions, as discussed below. Here, however, the focus is on fossil magma chambers and volcanoes as elastic inclusions.

In central Iceland, above the centre of the Iceland Mantle Plume, is a high density of active polygenetic (central) volcanoes, most of which are thought to have collapse calderas (Fig. 16). Many of these volcanoes appear to have dense swarms of inclined sheets and radial dikes, and all are associated with a gravity anomaly, suggesting sheet intrusions and large plutons (Fig. 17). The plutons, swarms of sheet intrusions and, for many of the volcanoes, caldera in-fills make the models of elastic inclusions appropriate.

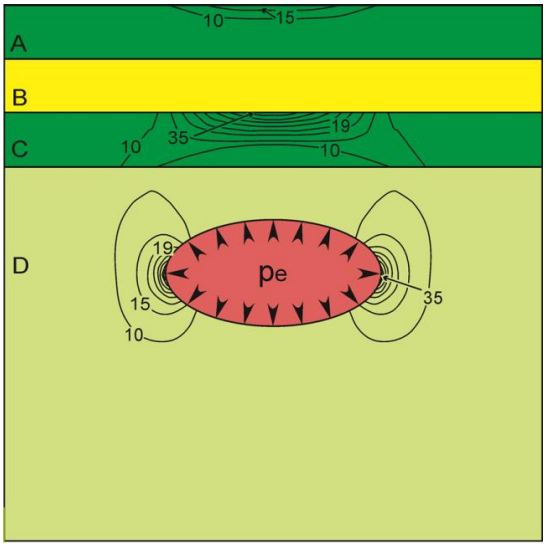

Fig. 12. Tensile stress gradients around a magma chamber modelled as an oblate ellipsoidal cavity in a layered crustal segment. In this numerical model there are three layers above the unit hosing the chamber. Layers A and C are stiff with a Young's modulus of 100 GPa, whereas layer B is compliant (soft) with a Young's modulus of 1 GPa. Layer D, which hosts the chamber, is moderately stiff with a Young's modulus of 40 GPa. The only loading is magmatic excess pressure in the chamber of 10 MPa. The gradient (of σ_3 in mega-pascals) shown at the tips of the chamber is from 35 MPa to 10 MPa, but it decrease further away (not shown) from the tips. The stiff layers A and C also concentrate stresses, but the soft layer B suppresses stresses, so that the vertical stress gradient through the layers is not a smooth curve but with abrupt changes at layer contacts.

All the volcanoes in central Iceland are subject to extension related to the spreading vector (Fig. 16). The appropriate loading due to the spreading vector and applied to these volcanoes, modelled as elastic inclusions, is here regarded as tensile stress of 5 MPa, which is similar to the typical in-situ tensile strength of the crust (Gudmundsson, 2011). The resulting stress fields show that tensile stress generally decreases away from the volcanoes/inclusions (Fig. 18), as has been observed in the models above and as is in harmony with Eqs 7-10.

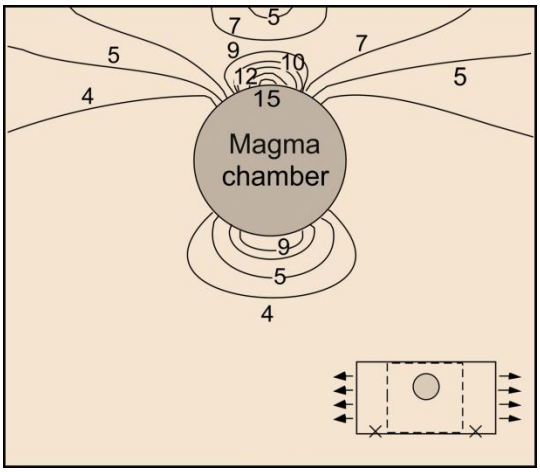

Fig. 13. Tensile stress gradients around a magma chamber of circular vertical cross-section subject to remote horizontal tensile stress (such as in a rift zone) of 5 MPa as the only loading (cf. Gudmundsson, 2020). The chamber is located in a homogeneous, isotropic crustal segment. In this numerical model the stress contours show σ_3 in mega-pascals. The gradients shown here range from 15 MPa (around the part of the chamber closest to the free surface) to 4 MPa, but the stresses diminish further with increasing distance from the chamber.

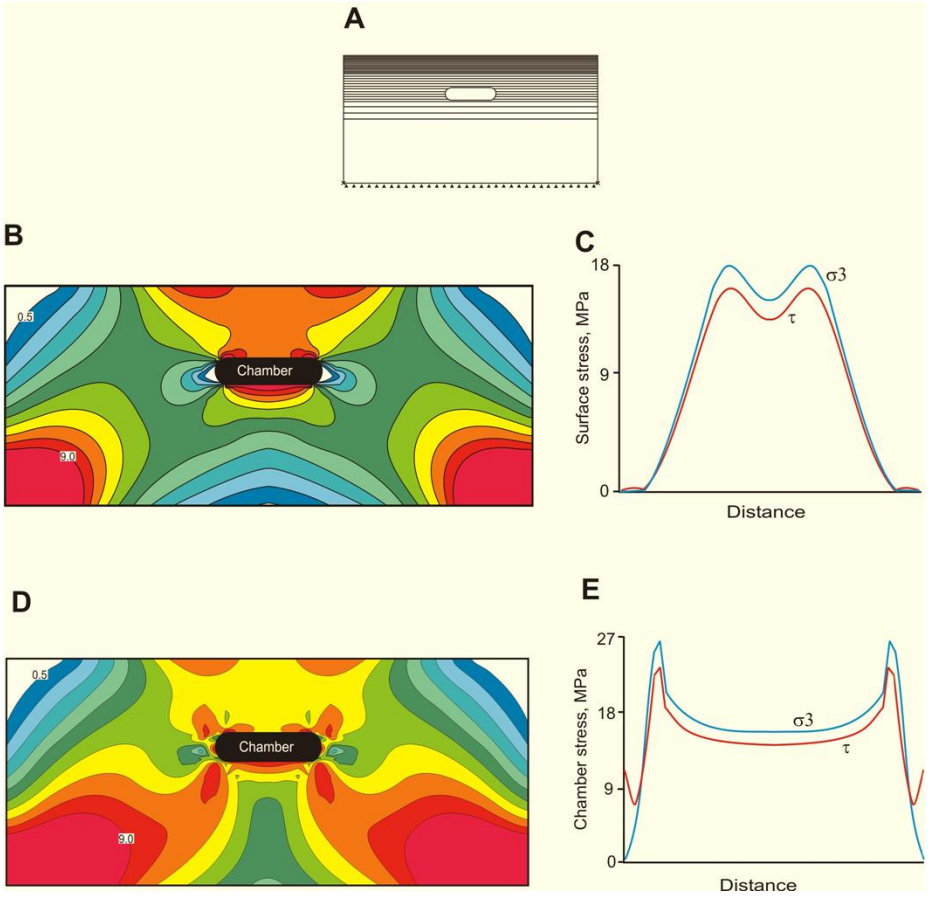

Fig. 14. Tensile stress and shear stress gradients around a sill-like magma chamber in a homogeneous, isotropic crustal segment with a stiffness of 40 GPa and a Poisson's ratio of 0.25 (cf. Gudmundsson, 2020). The only loading is a doming stress which is attributable to magmatic pressure increase of 10 MPa in a large magma reservoir assumed to be at the bottom of the segment. The segment is 20 km thick and 40 km wide. The chamber is located at 5 km depth and is 8 km wide and 2 km thick. All stresses are given in mega-pascals. (a) The basic configuration of the numerical model. (b) Contours of the tensile stress σ_3 around the magma chamber. (c) Tensile stress σ_3 and von Mises shear stress τ at the free surface above the magma chamber (surface of a volcano or a rift zone). (d) Contours of the von Mises shear stress τ around the magma chamber. (e) Tensile σ_3 and shear τ stress at the upper boundary of the magma chamber.

There are, however, some special features of the stress gradients here that can be related to some of the volcanoes/inclusions being comparatively close to each other. Thus, zones of high tensile stress exist between the two calderas of Kverkfjöll (Figs 17 and 18), as expected since they belong to the same volcanic system. But there are also zones of high tensile stress between Grimsvötn and Thordarhyrna and, to a lesser degree, between Bardarbunga and Grimsvötn and these belong to different volcanic systems. (There is also a high-stress zone between Grimsvötn and Thordarhyrna, but again these belong to the same system.) Zones of high tensile stress concentration between volcanoes modelled as elastic inclusion indicate that dikes and faults may be shared between some of the volcanoes (Gudmundsson and Andrew, 2007).

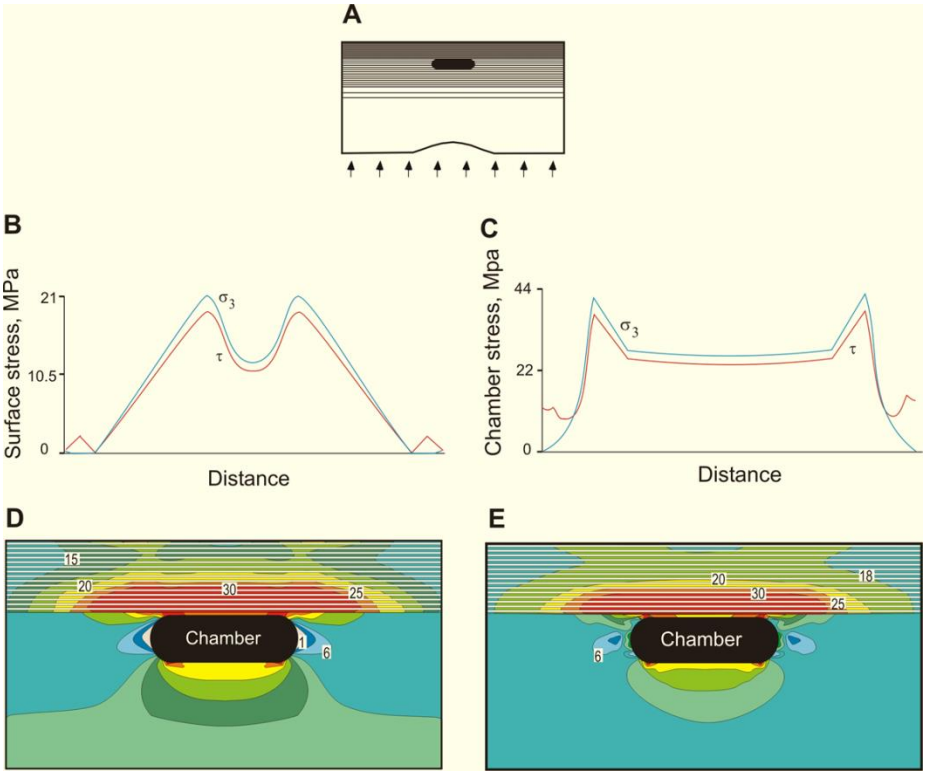

Fig. 15. Tensile stress and shear stress gradients around a sill-like magma chamber in a layered crustal segment (cf. Gudmundsson, 2020). In this numerical model the chamber is 8 km wide and 2 km thick and located at 3 km depth in a 20-km-thick and 40-km-wide crustal segment. The only loading is a doming stress (due to magmatic pressure increase in a reservoir at the segment bottom) of 10 MPa. The rock unit hosting the chamber has a Young's modulus of 40 GPa, whereas the uppermost 3 km of the crustal segment, constituting the roof of the chamber, consist of 30 layers of alternating Young's modulus of 1 GPa and 100 GPa. All stresses are given in mega-pascals. (a) The basic configuration of the numerical model. (b) Contours of maximum principal tensile stress σ_3 around the magma chamber. (c) Tensile stress σ_3 and von Mises shear stress τ at the free surface above the magma chamber (surface of a volcano or a rift zone). (d) Contours of von Mises shear stress τ around the magma chamber. (e) Tensile σ_3 and shear τ stress at the upper boundary of the magma chamber.

Stress gradients around dikes and sills

Dikes, inclined sheets, and sills affect surrounding stresses primarily in two ways: by increasing compressive (and shear) stresses in the walls of their host rock and by increasing tensile (and shear) stresses at the tips of their segments. Here we focus on dikes. We first discuss the induced stresses at the dike tips and then those in the dike walls before we briefly discuss the stresses around sills and those associated with sill-fault interactions.

Consider the stress field of a dike close to a shallow magma chamber as seen in plan view (Fig. 19). Fig. 19a shows that the tensile stress induced by the dike is primarily at its lateral tips, in the so-called process zone (Gudmundsson, 2011). The highest stress shown at the dike tip is only 10 MPa, because that is close to the maximum tensile strength that the crustal layers have - the values are most commonly 2-4 MPa, while the maximum measured in-situ tensile strength is about 9 MPa (Gudmundsson, 2011). Thus, the maximum tensile stress at the dike tip in nature is unlikely ever to exceed about 10 MPa, even if the theoretical tensile stress calculated numerically is much higher.

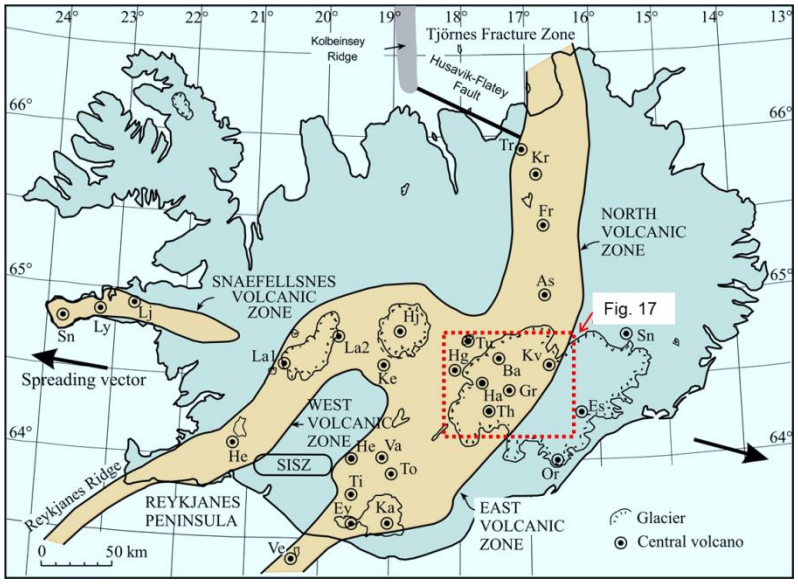

Fig. 16. Outline of the main geological features of Iceland. The active volcanic zone (brown) is divided into four subzones, namely: the North Volcanic Zone, the East Volcanic Zone, the West Volcanic Zone (a part of which is the Reykjanes Peninsula), and the Snaefellsnes Volcanic Zone. All the main active polygenetic (central) volcanoes are indicated (the names of the volcanoes are provided in Gudmundsson and Andrew, 2007). The details of those in the red-dotted rectangle are in Fig. 17 (where their names are also provided). Also shown are the Husavik-Flatey Fault, a transform fault that connects the North Volcanic Zone with the mid-ocean Kolbeinsey Ridge and the South Iceland Seismic Zone (SISZ – this is the central part of the zone which extends further north and south), a transform zone located between the East Volcanic Zone and the West Volcanic Zone. Both zones are characterised by large-scale strike-slip faulting, whereas the volcanic zones are characterised by large-scale normal faulting (and, of course, volcanic fissures).

Figure 19a also shows that outside the dike tips there is no tensile stress in the walls of the dike. This follows because the overpressure (driving pressure) of the magma in the dike induces compressive stress in the walls of the dike-fracture. This is seen in Fig. 19b where there is an induced (by the magmatic overpressure) horizontal compressive stress around the dike. The trajectories (ticks) of the maximum induced horizontal stress around the dike (Fig. 19d) show that they are mostly perpendicular to the dike next to it, but change direction somewhat with distance from the dike, partly because of mechanical interaction between the dike and the magma chamber. To complete the picture of the stress gradients and general variation close to the dike, Fig. 19c shows the von Mises shear stress around the dike. As for the tensile stress, the highest shear stresses are at and close to the lateral tips of the dike, and diminish with distance from tips.

For all the stress fields in Fig. 19, there is mechanical interaction between the regional dike and the shallow magma chamber. This follows because the chamber, modelled here as a circular hole in plan view, also concentrates stresses that interact with those induced by the dike. The reason I include the chamber here is, first, to show a common situation where a regional dike is close to a shallow magma chamber and, second, to put the stress fields shown for circular hole above (Figs 1-2, 6-7) into a common volcanotectonic context.

So far we have discussed only the stresses around a dike in plan view. In a vertical section, that is, along the dip-dimension of the dike, the stresses and stress gradients are very similar

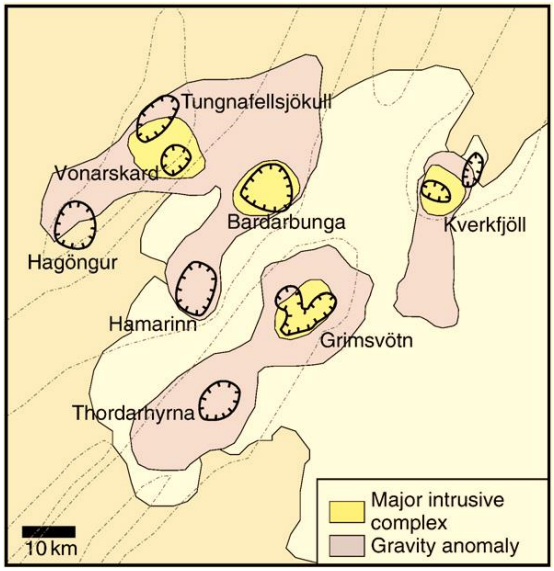

Fig. 17. Map showing the central volcanoes within the dotted rectangle in Fig. 16 and modelled numerically in Fig. 18. Also shown are the swarms of dikes and inclined sheets (marked as intrusive complexes) underneath and between the central volcanoes. The high density of central volcanoes in this part of Iceland is partly due to this part of the country being located above the centre of the Iceland Mantle Plume. The Vatnajökull ice sheet is shown in light colour. The volcanic systems marked by dashed lines. Modified from Andrew and Gudmundsson (2008).

to those shown in the plan view (Fig. 19). More specifically, there is induced compressive stress in the walls of the dike, except at the tips (top and bottom) where tensile and shear stresses dominate (in the process zone).

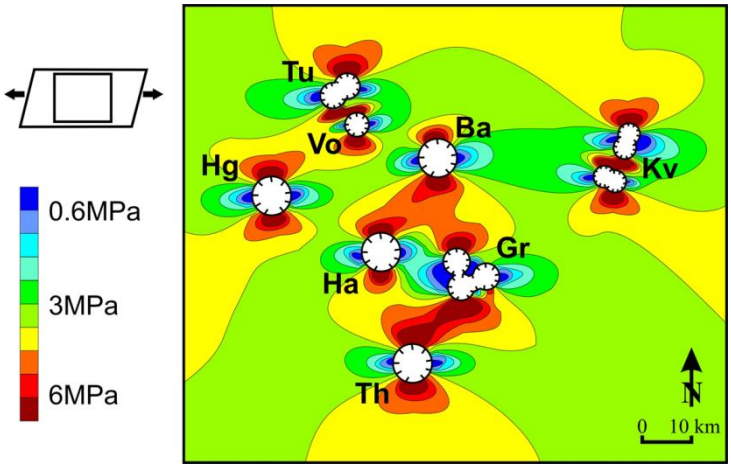

Fig. 18. Tensile stress gradients around and between central volcanoes (many with collapse calderas) in central Iceland (cf. Figs 16 and 17). The tensile stress σ_3 is given in in mega-pascals. In this numerical model the crust is assumed homogeneous and isotropic with a Young's modulus of 20 GPa and a Poisson's ratio of 0.25. The only loading is tensile stress of 5 MPa in the direction of the spreading vector (as indicated on the inset and shown in Fig. 16). The volcanoes are: Tu = Tungnafellsjökull, Vo = Vonarskard, Hg = Hagöngur, Ba = Bardarbunga, Ha = Hamarinn, Th = Thordarhyrna, Gr = Grimsvötn, and Kv = Kverkfjöll (cf. Gudmundsson and Andrews, 2007). The gradients decrease away from individual volcanoes but the stress magnitudes remain high between nearby volcanoes, particularly in zones that trend roughly perpendicular to the direction of the spreading vector (Fig. 16). The swarms of dikes and inclined sheets partly follow the stress-concentration zones between volcanoes.

Mechanical layering, however, can affect the stresses induced by dikes and other structures. In active volcanic zones, the layering (mostly of lava flows and pyroclastic and soil layers) is primarily subhorizontal so that the stress effects seen in at the surface (in the plan view) are minimal but commonly great as seen in vertical sections. Figure 20 shows the effects of mechanical layering on the induced stresses ahead of an upper dike (or any other fluid-driven fracture) tip. The layers are of contrasting Young's modulus or stiffness, and the tensile stresses concentrate in the stiff layers whereas the more compliant layers receive little if any tensile stress. This type of variation in induced stresses ahead of propagating dikes is very common and one reason for their comparatively slow vertical propagation and common arrest.

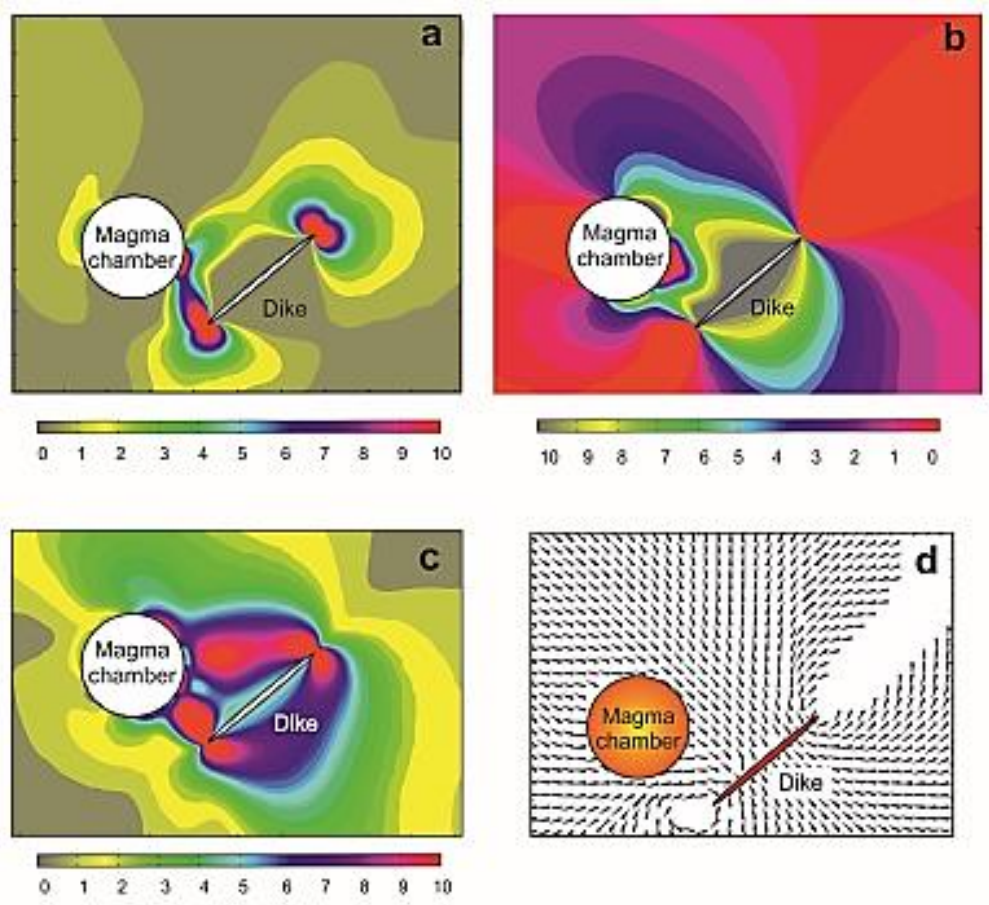

Fig. 19. Stress gradients around an active volcano, Bardarbunga (a collapse caldera, located in Figs 16-18), during dike emplacement associated with the 2014-15 eruption. The numerical models show the dike-induced stress around the Bardarbunga magma chamber during the early stages of the dike propagation. All the stresses are in mega-pascal. Tensile and compressive stresses have opposite signs, so that they are here shows as absolute values, but the increase in tensile (a) and von Mises shear (c) stresses are given the opposite direction on the scale (to the right) to that of the compressive stress (b). North is up on all the figures and the magma chamber is 10 km in diameter. Also shown are (d) the trajectories (directions) of σ_H (the maximum horizontal compressive stress). The stresses concentrate around the dike, particularly at its lateral tips, and also around the magma chamber so that the gradients vary in direction and the rate of decrease away from the main stress sources. Intensive faulting, normal, strike-slip, and reverse, occurred during the dike propagation (Gudmundsson et al., 2015), so as to gradually reduce the gradients.

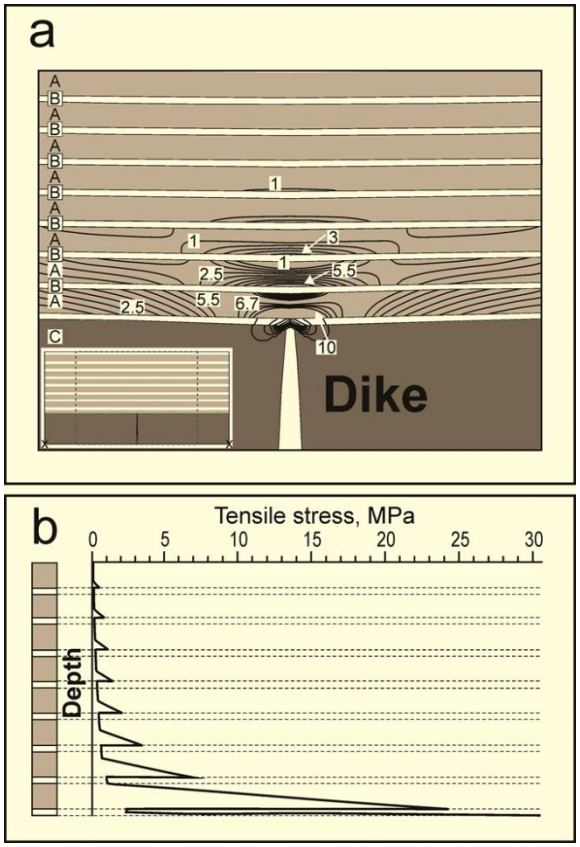

Fig. 20. Tensile stress gradient from the upper tip of a dike located in a layered crust with 10 MPa overpressure as the only loading. Above the tip of the dike, which is hosted by layer C (stiffness 40 GPa, Poisson's ratio 0.25 – as for all the layers) there are 16 layers; 8 stiff ones (100 GPa, marked by A) and 8 compliant ones (1 GPa, marked by B). The dike tip is 2 units below the surface (and touches the lowermost B layer), and each of the stiff layers has a thickness of 0.2 units, and each of the compliant layers a thickness of 0.05 units. Thus for a dike arrested with its upper tip at 500 m below the surface (as is common, e.g. during the November 2023 dike emplacement at Sundhnukur, Reykjanes Peninsula, Iceland) each of the thick layers would be 50 m and each of the thin layers 12.5 m – these are common thicknesses in a pile of lava flows and hyaloclastites such in the volcanic zones of Iceland (Gudmundsson, 2017). There are no weak mechanical contacts between the layers (they are assumed 'welded together'). The maximum dike tip stress is only 30 MPa because it is partly suppressed by the lowermost layer B. The tensile stresses peak in the lower parts of the A layers, but are very low in all the B layers, with no tensile stress reaches the surface (cf. Philipp et al., 2013).

Sills (Fig. 3) also induce stress concentrations and, thereby, stress gradients. As an example, consider a sill that is propagating laterally at the contact between mechanically dissimilar layers inside a graben (Fig. 21). The only loading is magmatic overpressure of 10 MPa which is supposed to drive the propagation of the sill towards the two normal faults that constitute the graben. In Fig. 21a the standard stress concentration and gradients are seen around the sill where the sill tips are comparatively far from the normal faults, so that the mechanical interaction is minimal. It follows that the stress field around the sill seen in Fig. 21a is very similar to that seen around an isolated sill, located far from any major geological structures and the free surface of the Earth. The main tensile stress concentration around the sill is at its tips – as is the case for dikes (Fig. 19) and decreases rapidly away from the tips. There is also a 'stress shadow', that is, increase in compressive stress in the host rock that constitutes the roof and the floor of the sill, as was observed for the walls of a dike (Fig. 19).

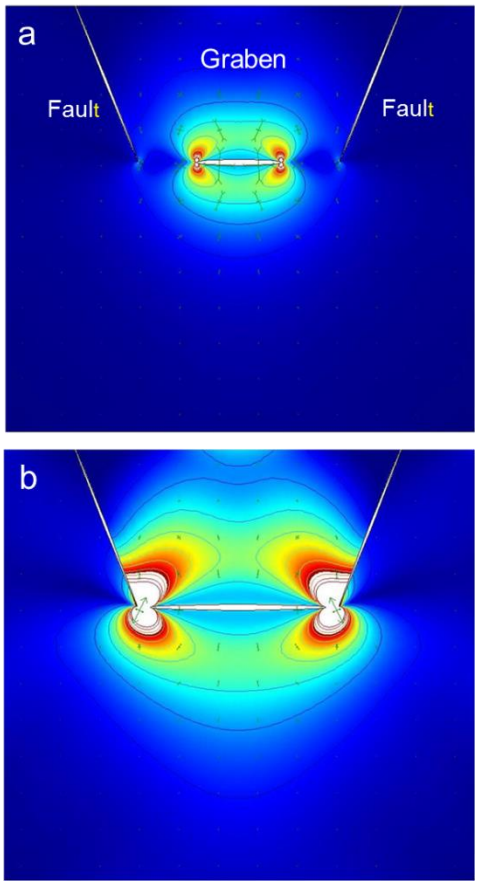

Fig. 21. Numerical model of the local stress field generated around a laterally propagating sill (a-b) towards the normal faults of a graben within which the sill is forming. The only loading is the sill's magmatic overpressure of 10 MPa. The host rock has a constant Young's modulus of 20 GPa (and a Poisson's ratio of 0.25). The contours show the von Mises shear stresses in mega-pascals (cf. Gudmundsson and Loetveit, 2012).

When the sill approaches the normal faults of the graben, however, the stress field changes somewhat (Fig. 21b). This is partly because active faults, as these are supposed to be, function as soft inclusions (with a comparatively low Young's modulus) and therefore suppress stresses – as is discussed below. As a consequence, very little tensile stress is transferred through the faults to the host rocks outside them (outside the graben). The tensile stresses thus become raised in a large area around the tips of the sill so as to spread out the process zone. The suppression of stresses by the faults is therefore entirely analogous to the suppression of stresses by compliant layers in a layered crust (Fig. 20). This brings us to the general effects of faults on stress gradients, to which we turn now.

Stress gradients around faults

Faults acting as elastic inclusions (Fig. 22) affect the local stress fields and gradients in two main ways, namely by increasing (concentrating) stresses and by suppressing stresses. In this way faults are entirely similar to rock layers of any kind. That is, layers or inclusions with a low Young's modulus suppress or dissipate stresses whereas layers or inclusions with high Young's modulus concentrate or raise stresses. While a fault is active, its core tends to be compliant (with a low Young's modulus) since it is mainly made of breccia, gouge, clay and other comparatively soft materials (Fig. 23). While the much thicker damage zone is

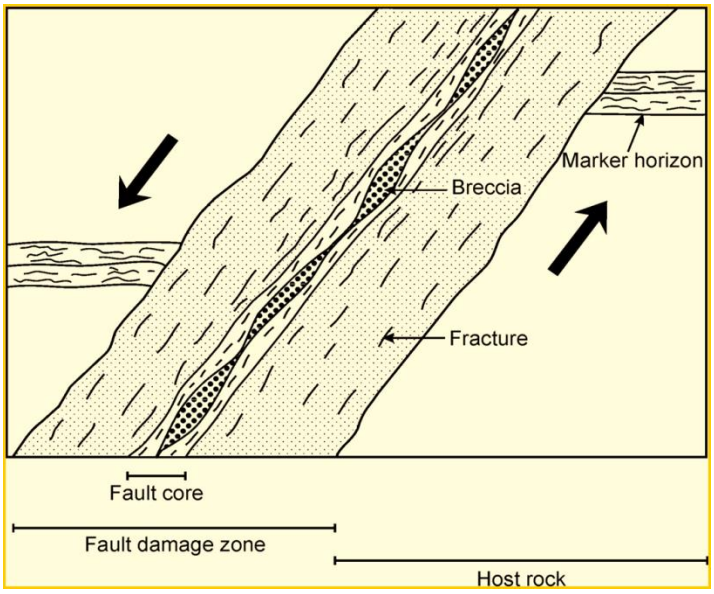

Fig. 22. Detailed internal structure of a fault, here a normal fault, which acts as an elastic inclusion (cf. Fig. 4). The internal structure of the fault is composed of two main mechanical units: a fault damage zone and a fault core. The core is composed of breccia, clay, fault gouge and other particulate materials. By contrast, the damage zone is primarily characterised by fractures whose frequency varies – and generally decreases in an irregular fashion – away from the contact between the damage zone and the core. When the fault is active, the damage zone and core act as a soft elastic inclusion. In inactive faults, however, the stiffness of the core and damage zone increases because of secondary mineralisation and compaction and may eventually become higher than that of the host rock – in which case the inactive fault acts as a stiff elastic inclusion.

normally stiffer than the core, the damage zone is characterised by tectonic fractures whose frequency normally increases irregularly towards the contact with the core (Gudmundsson et al., 2010). Fractured rocks normally have a lower Young's modulus that non-fractured rocks of the same lithology (Gudmundsson, 2011). Thus, both the core and the damage zone of an active fault are usually more compliant than the host rock; therefore, an active fault acts as a soft inclusion (Fig. 22).

As an example, consider the stress fields and gradients around the fault in Fig. 24. The fault is a strike-slip fault, is active, and acts as a soft inclusion inside the stiffer host rock. The fault core is composed of breccia and other soft materials and is assigned a Young's modulus of 0.1 GPa. But inside the core is the fault plane itself (where the main slip within the core takes place) which is modelled as a spring of stiffness 6 MPa m^{-1}. The damage zone is much thicker than the core, but can be divided into two subzones based on the fracture frequency. Thus, the inner zone, with a much higher frequency, has a Young's modulus of 1 GPa, whereas the outer zone has a Young's modulus of 10 GPa. Both of these zones are much more compliant than the host rock whose Young's modulus is 50 GPa. The only loading of the fault zone is oblique horizontal compressive stress of 15 MPa. All these values are based on field and laboratory studies, originally for a fault zone in West Norway (Gudmundsson et al., 2010).

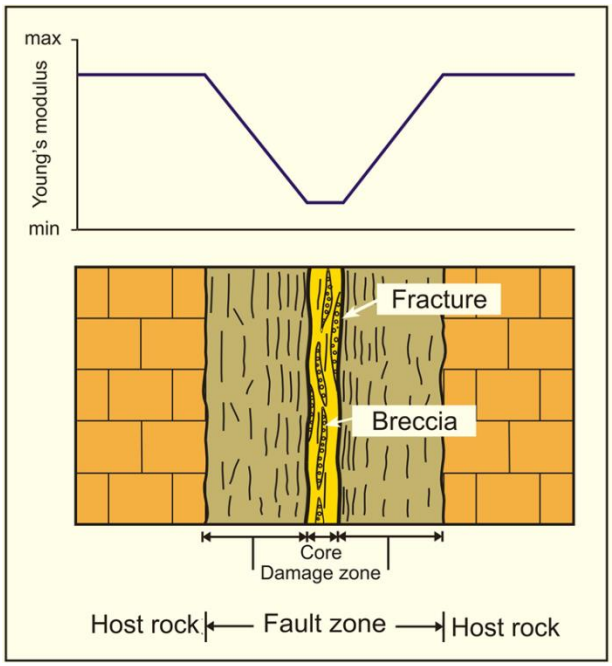

Fig. 23. So long as a fault is active, its core and damage zone have lower stiffness than that of the surrounding host rock. This is indicated here in a generalised way, showing a linear decrease of Young's modulus from the host rock through the damage zone and to the core. In nature the variation in Young's modulus is more complex; for example the damage zone commonly shows a great variation in fracture frequency, hence in effective Young's modulus (Gudmundsson, 2011), so that it forms subzones (Figs 24 and 25).

The results (Fig. 25) show that von Mises shear stress decreases from the host rock into the fault zone. More specifically, the fault zone is a zone of lowered shear stress. It follows that the shear-stress gradient, for these mechanical properties and loading, is from lower stresses inside the fault zone to higher stresses outside the fault zone. This may become as a surprise to some. But active fault zones are simple mechanically weak structures. They tolerate less shear stress before failure than the less fractured host rock. Active fault zones of this kind therefore slip at low driving shear stresses and thereby keep the potential stresses at and in their surroundings comparatively low – while the fault permeability is comparatively high (Barton et al., 1995; Townend and Zoback, 2000). It should be noted, however, that this applies only to established fault zones with mechanically weak cores and damage zones. The results are different when a new fault is being formed. Furthermore, the cores and damage zones of old inactive fault zones commonly become as stiff, or stiffer, than the host rock. This is primarily because of secondary mineralisation and compaction in the fault zones. The result is that they may then act as stiff elastic inclusions (Figs 4 and 22) whose stresses, under renewed loading (if that happens), may be higher than that of the surrounding rocks. But these are not discussed further here, where the focus is on active tectonics and associated brittle deformation, to which we turn now.

Stress gradients and brittle deformation

Crustal rocks deform when stresses reach critical values. Where the temperatures are comparatively low, or the strain rates are high, or both, the deformation is primarily brittle. At high temperatures, low strain rates, or both, the deformation may be primarily ductile. For

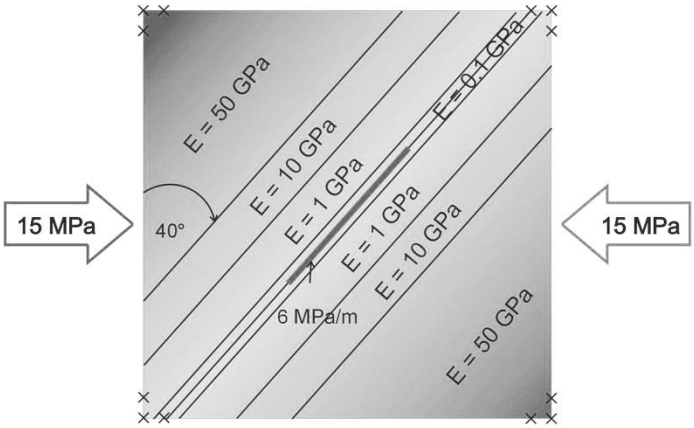

Fig. 24. Set-up for the fault model in Fig. 25. The data derive from a large fault in West Norway (Gudmundsson et al., 2010) where the fracture frequency in the innermost 20 m of the damage zone is nearly double that in the outer part. For the inner damage zone a Young's modulus of 1 GPa is used whereas for the outer damage zone a Young's modulus of 10 GPa. Additionally, at 80 m from the core, which as a Young's modulus of 0.1 GPa (the fault plane itself being modelled as a spring with a stiffness of 6 MPa m^{-1}), the host rock (gneiss) takes over with a Young's modulus of 50 GPa. The fault strike is N40°E, whereas the loading, inferred from stress data in Norway, is E-W compression.

both brittle and ductile crustal behaviour, the deformation induced by the stresses results stress changes (mostly lowering of stresses in concentration areas/zones) and, thereby, in the reduction of the local stress gradients. Here the focus is on the brittle deformation, so all the examples are on brittle structures.

The main brittle structures whose formation and development contributes to the reduction of stress gradients are rock fractures. These are geometrically of various types that range in outcrop size from cm-long joints to km-long extension fractures and faults. The longest fractures, which are best seen on satellite images, reach tens (and some hundreds) of kilometres.

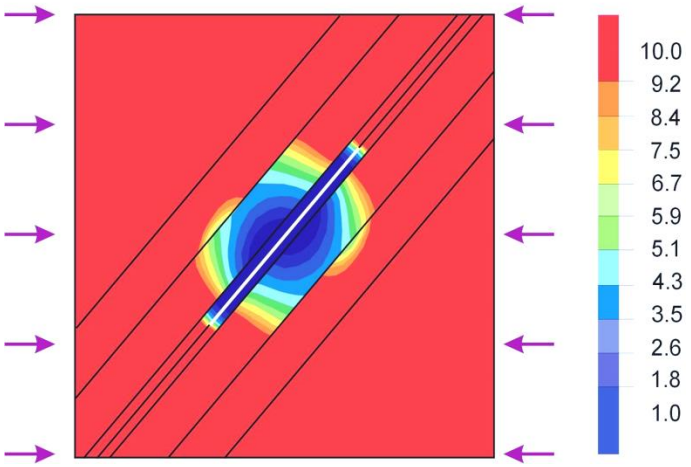

Fig. 25. Numerical model of the fault in Fig. 24. The contours show von Mises shear-stress concentration (in MPa) around the fault. The fault core and inner damage zone have comparatively low shear stress concentration, 1–5 MPa, although high enough for fault slip. The outer damage zone has comparatively high shear stress. There is thus, as expected, a stress gradient from the compliant core and the comparatively compliant inner damage zone to the outer damage zone and to the host rock (Gudmundsson et al., 2010). Yet, despite the low stress values in the core and the inner damage zone, fault slip occurs primarily in these zones because they are mechanically weak (with low shear strength).

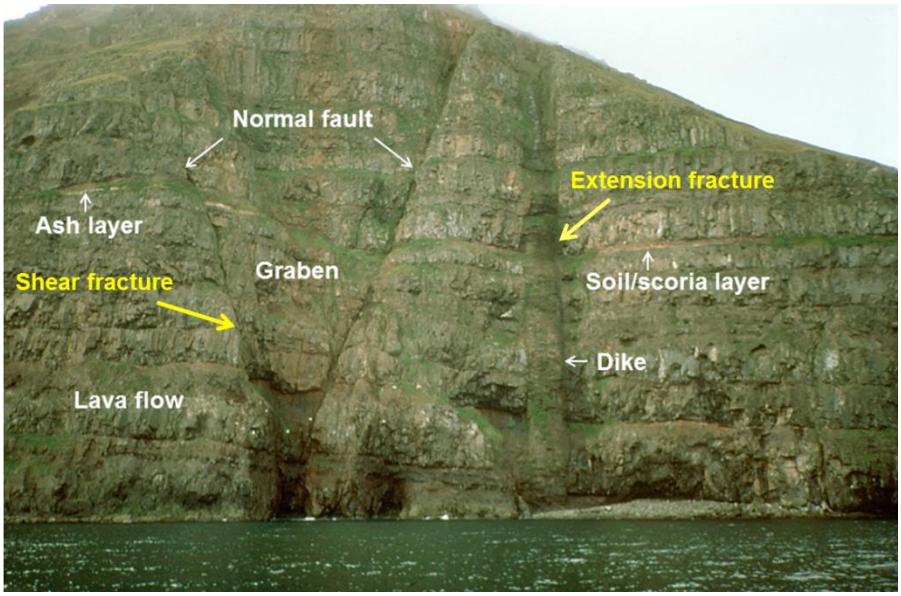

Fig. 26. Two main mechanical types of rock fractures are shear fractures and extension fractures, both of which are seen here in a 120 m high sea cliff, composed of 12-Ma basaltic lava pile in North Iceland. The shear fractures are normal faults, which here constitute a graben whose tip is at sea level (which is at about 1500 m depth below the original surface of the lava pile). The extension fracture is here a dike, a hydrofracture (a fluid-driven fracture), of thickness 6 m.

In addition to joints, the main types of outcrop-scale fractures are as follows: mineral veins, dikes (and sills and inclined sheets), tension fractures, and faults. Faults are classified into two main groups, namely dip-slip faults and strike-slip faults. Dip-slip faults can be further divided into normal faults and reverse faults (if steeply dipping) and thrust faults (if gently dipping). Strike-slip faults are also divided, depending on the sense of movement, into dextral (right-lateral) and sinistral (left-lateral). These are all common terms from structural geology and volcanotectonics (Gudmundsson, 2011, 2020). When rock fractures are modelled using fracture-mechanics concepts, the models used are based on the type of movements of the fracture walls (referred to as mode I, mode II, mode III, or mixed mode) and the location of the fracture in relation to any free surface (rock surface in contact with fluid) as through-cracks, part-through cracks, and interior cracks.

Fortunately, even if the detailed geometric classification of fractures is somewhat intricate, the mechanical classification of rock fractures is simple. This is because there are only two mechanical types of rock fractures, namely extension fractures and shear fractures (Fig. 26). In an extension fracture the fracture plane is perpendicular to the least principal stress σ_3 and parallel with the maximum σ_1 and intermediate σ_2 principal stresses. When an extension fracture forms, the fracture simply opens up – the walls just separate. This means that there is no wall-parallel movement, only wall-perpendicular movement. This is seen for tension fractures (Fig. 27) and dikes (Figs 26 and 28) in the field. Thus, extension fractures themselves are of two basic types: tension fractures (Fig. 27) and fluid-driven fractures, also called hydrofractures, of which dikes are an example (Figs 26 and 28). Tension fractures are always shallow (usually not deeper than a few hundred metres in the earth's crust) since they

Fig. 27. Tension fracture (named Flosagjá, cf. Fig. 37) with a maximum opening displacement (aperture) of 15 m in a basaltic lava flow, of Holocene age, in the Thingvellir Graben in the West Volcanic Zone of Iceland (Fig. 16). View northeast, the fracture is seen from the air in Fig. 37 (cf. Gudmundsson, 2017).

require that σ_3 becomes negative in the absence of fluid pressure, and this can happen only close to the surface, mostly in active rift zones. Hydrofractures, however, can form at any depth. This follows because it is the fluid overpressure that ruptures the rock and allows the fracture to propagate. More specifically, the roof of the source ruptures and a hydrofracture becomes injected when the following conditions are satisfied (Gudmundsson, 2022a):

$$p_l + p_e = \sigma_3 + T_0 \tag{11}$$

Here p_l is the lithostatic stress (also named overburden pressure) at the location of rupture and fracture initiation at the hydrofracture source boundary and p_e is the excess fluid pressure in the source. Furthermore, σ_3 is the minimum compressive (maximum tensile) principal stress, and T_0 the local in situ tensile strength at the rupture site. Once the hydrofracture begins to propagate upwards towards the surface, from its source, buoyancy becomes into play through the following equation which presents the overpressure p_o in a fluid-driven fracture:

$$p_o = p_e + (\rho_r - \rho_f)gh + \sigma_d \tag{12}$$

where ρ_r is the average host-rock density, ρ_f is the average fluid density, g is the acceleration due to gravity, h is the dip-dimension of the hydrofracture, and σ_d is the differential stress (the difference between the maximum and the minimum principal stress) in the host rock

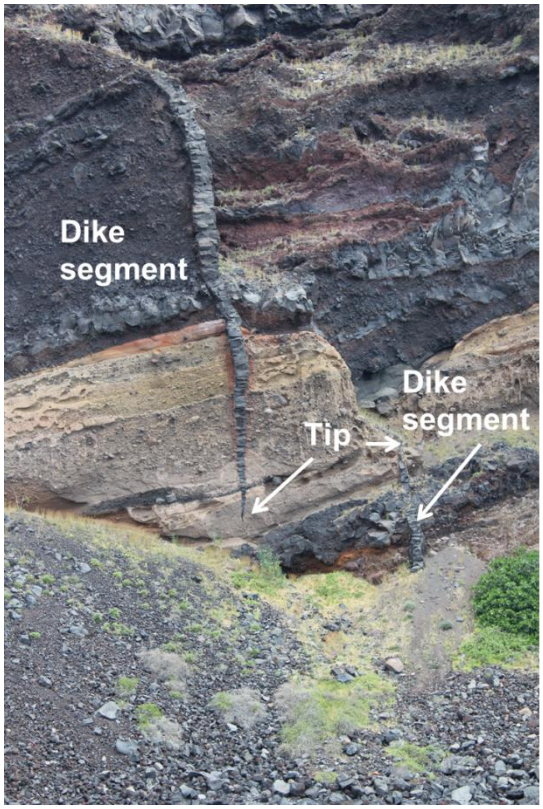

Fig. 28. Thin basaltic dike in the northern caldera wall of Santorini, Greece (located in Fig. 32). The upper segment shows the typical cross-sectional shape of a dike, namely a flat ellipse – an oblate ellipsoid in three dimensions. The maximum thickness of the upper segment is 1 m and it forms a part of a larger, segmented dike.

where the hydrofracture – such as a dike or a mineral vein - is studied in the field (or, for a feeder-dike, at the surface). The second term on the right-hand side of the equation is the buoyancy term. It combines the effect of the difference in density between the host rock and the hydrofracture fluid, $(\rho_r - \rho_f)$, acceleration due to gravity, g, and the height or dip-dimension of the hydrofracture, h. The buoyancy term can be positive (average fluid density less than average rock density up to the point of interest along the hydrofracture), zero or neutral (average rock and fluid density the same), or negative (average rock density less than average fluid density). The overpressure in a fluid-driven fracture reduces the stress difference, the stress gradient, in the crustal segment though which it propagates, as discussed in more detail below.

Shear fractures in the earth's crust are primarily faults, although some joints may also be shear fractures. As indicated above, the main classes of faults are two types of dip-slip faults, and two types of strike-slip faults, while some faults are neither pure dip-slip nor strike-slip faults, but rather oblique-slip (Fig. 29). The local stress field associated with the different types of faulting (Fig. 30) is an indication of how faulting affects stress gradients.

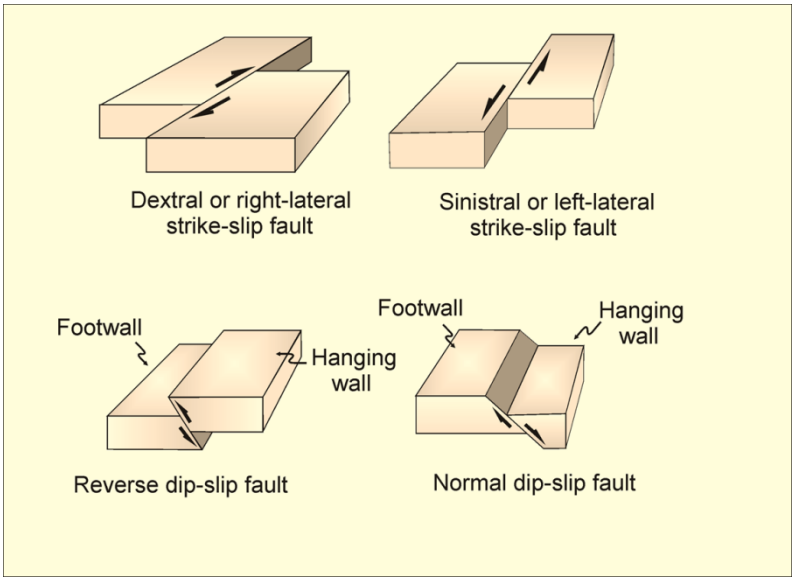

Fig. 29. Main types of faults are strike-slip (dextral and sinistral) and dip-slip (reverse and normal). A reverse fault with a dip of less than 45° is referred to as thrust fault. Some faults are neither pure dip-slip nor strike-slip faults, but rather oblique-slip.

Consider first normal faulting. Here the maximum compressive principal stress, σ_1, is vertical, and the minimum compressive (maximum tensile) principal stress, σ_3, is horizontal and in a direction perpendicular to the strike of the fault. The effect of fault movement is thus to cause contraction in the vertical direction, that is, in the direction of σ_1, and expansion in the horizontal direction, that is, in the direction of σ_3. The overall result is that the magnitude of σ_1 becomes reduced whereas the magnitude of σ_3 increases, bringing the state of stress closer to isotropic (also known as hydrostatic) and, thereby, diminishing the associated stress gradient.

The stress change associated with normal faulting can perhaps be more easily visualised when we consider normal faults that constitute the boundary faults of a graben (Fig. 31). Clearly, when the rock body between the inward-dipping normal faults subsides, namely the rock body constituting the graben, the shape of the down-moving wedge means that there builds up horizontal compressive stress in the adjacent walls. The subsidence, driven by gravity, normally results in reduction of the difference between the original vertical σ_1 and the horizontal σ_3 so that they become close to equal in magnitude (and, occasionally, the original horizontal σ_3 may become, temporarily, greater in magnitude than the original vertical σ_1, in which case the principal stresses swap). The overall result is normally that all the principal stresses become close to equal, meaning that the stress field becomes isotropic/hydrostatic, thereby levelling out the stress gradient.

Consider next reverse faults (named thrust faults if the dip is small). Here the maximum principal stress σ_1 is horizontal and perpendicular to the strike of the fault, while the minimum principal stress σ_3 is vertical (Fig. 30). Since σ_1 is horizontal stress, the response of the crust during faulting is shortening (and thickening) in a direction parallel with σ_1. This means that as a consequence of the displacement the magnitude of the original horizontal σ_1

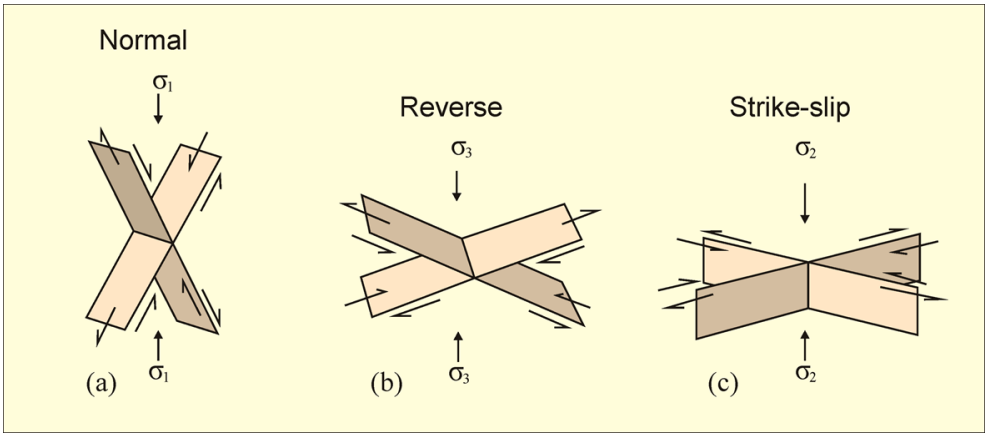

Fig. 30. Standard (Anderson's) classification of faults in relation to the local stress field. The principal stresses, $\sigma_1 \geq \sigma_2 \geq \sigma_3$, are, by definition, orthogonal. The vertical principal stress is σ_1 for normal faulting (so that σ_2 and σ_3 are horizontal), σ_3 for reverse faulting (so that σ_2 and σ_1 are horizontal), and σ_2 for strike-slip faulting (so that σ_3 and σ_1 are horizontal).

reduces whereas the magnitude of the original σ_3 increases. Thus, again the result of faulting is to bring the state of stress closer to isotropic/hydrostatic and, thereby, reduce the original stress gradient.

For strike-slip faulting, both dextral and sinistral, the result of fault displacement is again reduction in the magnitude of the original σ_1 and increase in the original magnitude of σ_3, both of which are horizontal (Fig. 30). The result of strike-slip faulting is therefore the same as in the case of normal and reverse faulting, namely the fault displacement tends to bring the state of stress closer to isotropic and, thereby, reduce the original stress gradient.

Before we turn to the application of these results, it should be mentioned that in tectonically and/or volcanically active areas, while dike emplacement and faulting tend to diminish the local stress gradient, the large-scale processes tend to increase the gradient again. The large-scale processes involved here are primarily plate-boundary processes. Thus, plate-boundary and related large-scale processes tend to build up or maintain stress gradients while brittle deformation seeks to diminish or destroy stress gradients.

Application

To illustrate how brittle deformation may reduce stress gradients, we shall discuss several examples from the field. The examples chosen are from island of Santorini in Greece and from Iceland. Since outcrop-scale brittle deformation is primarily through fracture formation, the focus is on fractures. In particular, the application includes dikes in Santorini and faults in Iceland. The focus is on quantitative data obtained by direct measurements of the structures in the field.

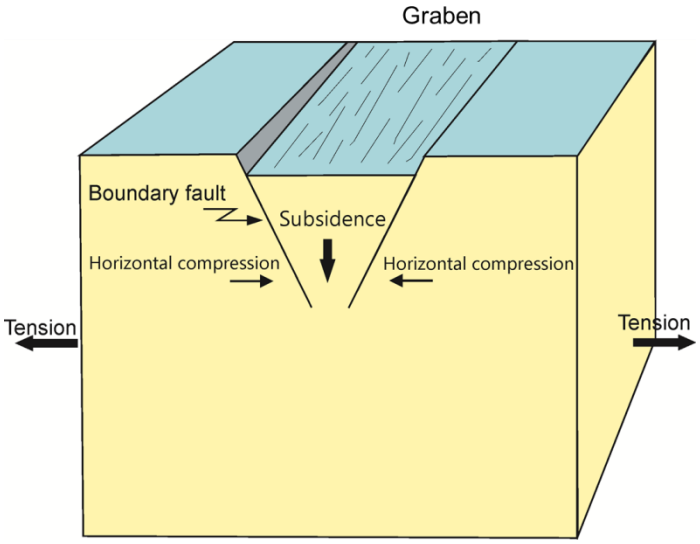

Fig. 31. Vertical displacement, subsidence, of a graben in a volcanic rift zone may temporarily alter the local stress field so as to induce horizontal compressive stress in a direction perpendicular to the strike of the graben. Thus, following graben subsidence the local stress field may for a while be so that σ_1 is horizontal, thereby encouraging injected dikes to become arrested or deflected into a sill (cf. Fig. 21).

Dike injection in Santorini

There is a dike swarm in Santorini that is particularly well exposed in the inner sea-cliffs, a caldera rim, in the northern part of the island (Figs 28 and 32). These dikes and related structures have been described in detail (Browning et al., 2015; Drymoni et al., 2020, 2021) and so has the geological framework of Santorini (Friedrich, 2009; Drymoni et al., 2022). The dikes strike mostly north-northeast, with smaller group of dikes striking north-northwest. Many of the dikes are likely to be radial, that is, injected from a shallow magma chamber rather than a deep-seated reservoir (Gudmundsson, 2020). Geological and geodetic data suggests a shallow chamber beneath Santorini at a depth of about 4 km (Fig. 33; Browning et al., 2015). Radial dikes tend to be thinner and somewhat more evolved than regional dikes (Gudmundsson, 2020). The composition of the dikes is primarily in the range from andesite to trachydacite.

The thickness of some 90 measured dike segments exposed in the caldera rims of Santorini ranges from 0.1 m to 8 m (Drymoni et al., 2020). The majority of the dikes are steeply dipping, that is, 91% dip in excess of 75°, and comparatively thin, with an arithmetic average thickness of 1.1 m. The thickness distribution follows roughly a negative exponential distribution (Browning et al., 2015), in line with the common dike-thickness distributions as discussed below.

Dike overpressure from its aspect ratio

To estimate the effects of dike emplacement on the local stress gradient, we proceed as follows. If the dimensions of the dike are known, that is, if either the strike-dimension or the dip-dimension (or both) are known in addition to the thickness, then the magmatic

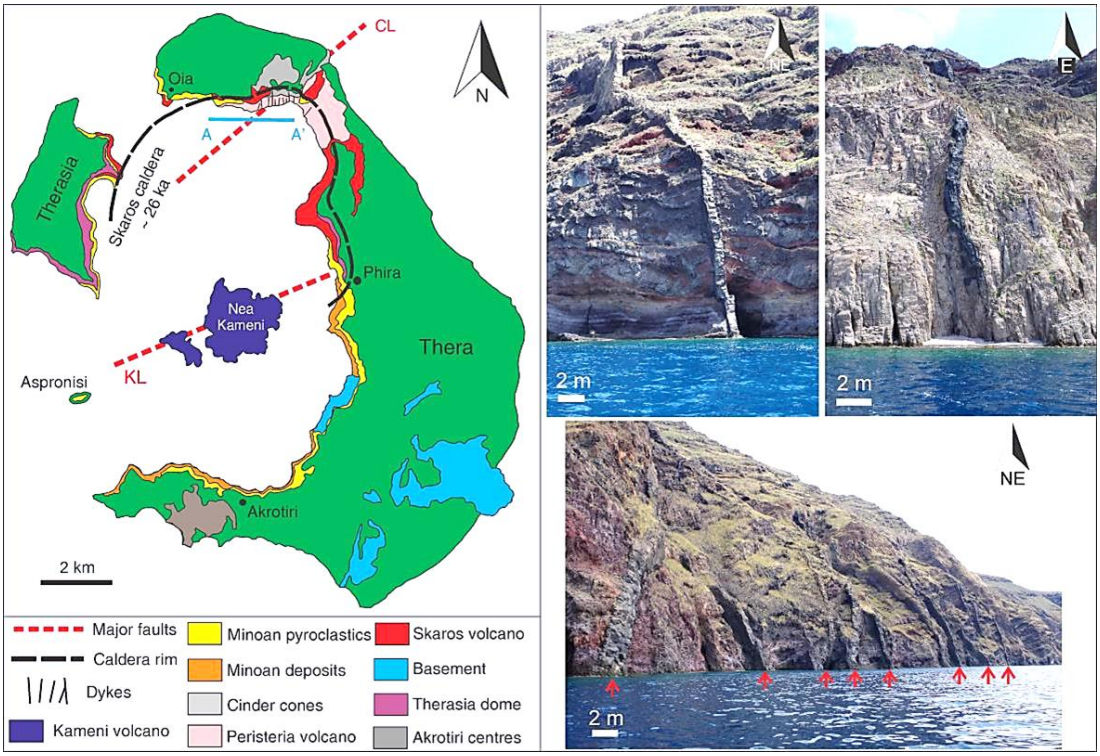

Fig. 32. Schematic geology of the island of Santorini (Greece). The caldera is indicated (including the inferred Skaros caldera rim), and so are the two main tectonic lineaments of Kameni and Coloumbo. The main dike swarm in the area is exposed (in the north) along the Skaros rim (the main profile measured is indicated as A-A', which also includes the dike seen in Fig. 28). On the photographs, dikes (many of which are arrested) are marked by red arrows. The geology, based on Druitt et al. (1999), and the dike data are from Browning et al. (2015).

overpressure p_o, which translates into added horizontal compressive stress in a direction perpendicular to the dike at a particular depth in the crust can be calculated using the following equation (Sneddon and Lowengrub, 1969; Gudmundsson, 2020):

$$p_o = \frac{\Delta u_I \; E}{2L\left(1-\nu^2\right)} \tag{13}$$

where Δu_I is the opening displacement of the magma-filled fracture (similar to the thickness of a later solidified dike), E is Young's modulus of the host rock, L is the dimension of the magma-filled fracture or dike being used (the smaller one of the dip-dimension and the strike-dimension), and ν is Poisson's ratio of the host rock. Thus, Eq. (13) can be used either to analyse the stress effect of the dike in a vertical section or, as is more common, in a lateral (plan-view) section. Notice that when estimating the overpressure from Eq. (13) the dimension used for L is normally the shorter of the dip-dimension and strike-dimension. The shorter one is the dimension that primarily affects the opening displacement (the thickness) of the dike and is referred to as the controlling dimension (Gudmundsson, 2020).

For an active dike (a dike that has just been emplaced during a dike-injection event), a magma-filled fracture, the approximate vertical and the lateral dimensions can often be

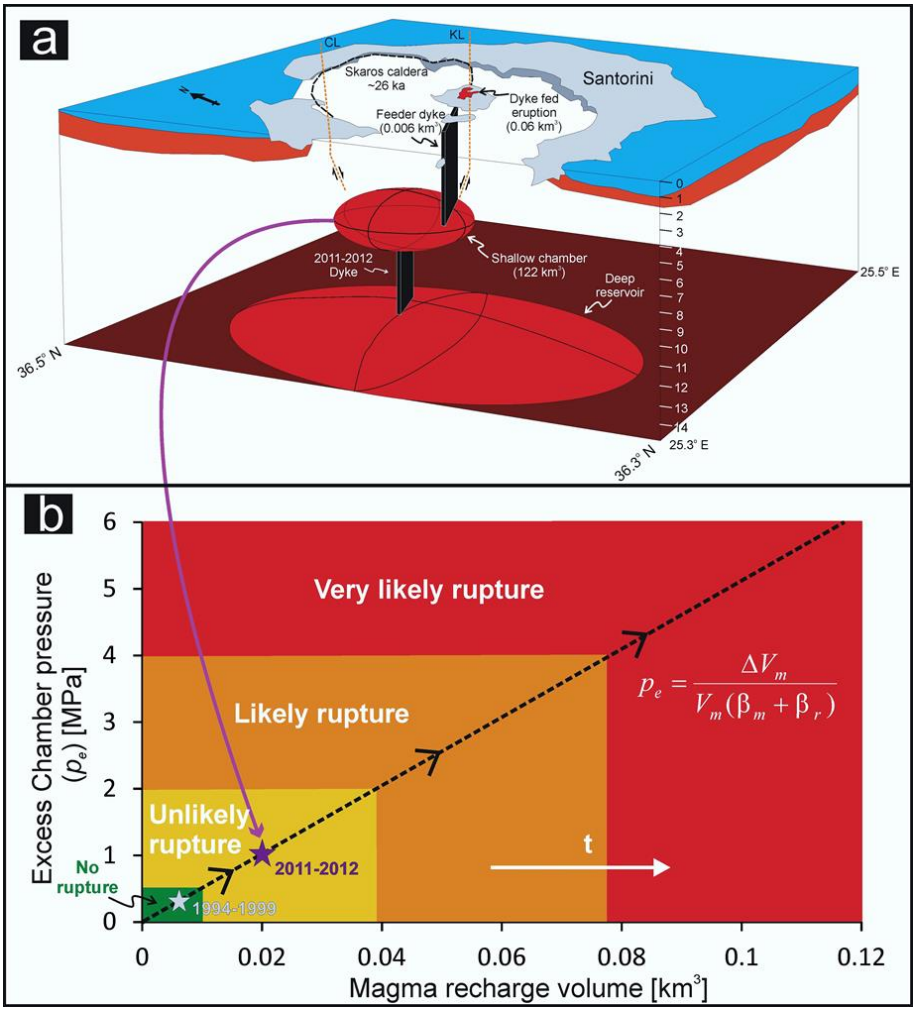

Fig. 33. Schematic illustration of (a) an inferred shallow magma chamber and a deeper source reservoir beneath Santorini and (b) the excess chamber pressure needed for chamber roof rupture and dike injection. (a) The shallow chamber is inferred to be at a depth of about 4 km and with a total volume of around 122 km^3. The maximum depth shown in the illustration is 15 km. (b) The diagram provides an estimate of the excess pressure (p_e) within the shallow magma chamber as a function of the volume of new magma (ΔV_m) supplied to the chamber by the deeper reservoir, based on the theory of poroelasticity (Gudmundsson, 2020). The likelihood of chamber roof rupture and dike injection (but not necessarily eruption) follows from the excess pressure in relation to the tensile strength of the roof rock. The model is applied to the unrest periods of 1994-99 and 2011-12 (indicated by stars on the diagram) both of which resulted in inflation but apparently no roof rupture with dike injection (modified from Browning et al., 2015).

inferred from seismic data. With additional information from geodetic data, the opening displacement (thickness) can then also be estimated. For a feeder-dike to a volcanic fissure, the strike-dimension of the fissure is normally easily measured, and the so is the opening displacement from geodetic data. For a frozen (solid) dike, the overpressure of its magma at the time of its emplacement, and at the particularly location of the dike exposure, can also be calculated provided the strike-dimension or dip-dimension can be estimated or measured. While the thickness of a solid dike is somewhat less than that of the original magma-filled dike-fracture, the difference between original opening and the thickness is so small (about 10%) that it can be regarded as included in the error of the field measurement of the dike thickness (Gudmundsson, 2020). Furthermore, the 10% error in opening estimates based on dike thickness is much less than the errors in most geodetic opening or thickness estimates of

active but arrested dikes. When elastic half-space dislocation models are used for the latter, as is common (e.g. Dzurisin, 2006; Segall, 2010), the error can easily reach 50% or more (Gudmundsson, 2020; cf. Bazargan and Gudmundsson, 2019, 2020).

If the depth to the source and the average host-rock and magma density are known, then the magmatic overpressure of an active dike can be estimated using Eq. (12). This equation can be used to estimate the overpressure for dikes arrested at any particular depth below the surface. Additionally, Eq. (12) can be applied to estimate the magmatic overpressure in a dike at any depth from its top – either the arrested tip at some depth in the crust or, in the case of a feeder-dike, from the surface fissure fed by the dike – down to its source. Magmatic overpressure using Eq. (12) can also be compared with that obtained from Eq. (13) in case all the relevant factors and parameters are known.

As indicated above, the buoyancy term $(\rho_r - \rho_f)gh$ plays an important role. Based on the density difference between the host rock and the fluid (here the magma), the term can be positive, zero, or negative. Therefore, this term can add to, or subtract from, the excess pressure p_e in the source at the time of rupture or, alternatively, have no effects on the excess pressure. The buoyancy comes into play, however, only after the dike has propagated for some vertical distance from its source up into the roof. This follows from the term *h*, namely the height of the dike above its source, that is, its dip-dimension. So long as the dike is propagating vertically, *h* is increasing and so is the buoyancy effect (positive or negative). But for a basaltic magma of density, say, 2750 kg m^{-3} and an average crustal density (for the roof of a shallow chamber) of, say, 2600 kg m^{-3} (Gudmundsson, 2020) the negative buoyancy effect attains 1 MPa only once the dike height or dip-dimension has reached some 680 m. Since the excess pressure p_e should be similar to the in-situ tensile strength of the roof and thus commonly 2-4 MPa, the negative effects of buoyancy on the overpressure do not become marked until the buoyancy term reaches at least 1 MPa, that is, at the dike height of around 680 m above the source in this example. Similar effects occur if the magma density is less than that of the average crustal density, but then the buoyancy pressure effect is positive and becomes added to that of the excess pressure.

The exposures of the dikes in Santorini are largely confined to the caldera rim, that is, to subvertical caldera walls (Figs 28, 32 and 33). This means that the lateral or plan-view exposure is limited. However, many of the dike segments studied are very thin, between 0.1 m and 0.5 m (Fig. 28; Browning et al., 2015; Drymoni et al., 2020), in which case Eq. (13) would imply that the strike-dimension is much shorter than the inferred depth to the source chamber (4 km) and thereby the controlling dimension.

The use of Eq. (13) for overpressure estimates of the Santorini dikes does require some general information about the aspect (strike-dimension/thickness) ratios from other dike swarms. There have been many measurements of the aspect ratios of dikes, most of the recent ones being summarised by Gudmundsson (2022b). In Iceland, for example, aspect ratios of regional basaltic dikes vary from about 300 to 1500, with an average of 803, and in Sudan

from 243 to 2331, with an average of 862 (Babiker and Gudmundsson, 2004). The most detailed recent data on aspect ratios of dikes, however, is provided by Masoud (2020), who studied three swarms of basaltic dikes in Sinai (Egypt) with average aspect ratios of 1543, 1540, and 2487. By contrast, and as expected, the average aspect ratio of felsic dikes in Sinai is lower or about 809 (Masoud, 2020).

All these results, as well as those on shallower radial dikes in El Hierro of the Canary Islands (Becerril et al., 2013) and in the caldera of Miyakejima Volcano in Japan (Kusumoto et al., 2013), suggest that dike aspect ratios give reasonable estimates of the magmatic overpressure at the time of dike formation. Even when the controlling dimension is only partially exposed, as is common and as applies to Santorini, it may be possible to use this method to estimate the magmatic overpressure at the time of dike emplacement (Biswas et al., 2023).

Using this method for the dikes on Santorini, Browning et al. (2015) show that even for the rather high aspect ratio of 1500, most dikes in Santorini would have the strike-dimension as their controlling dimension. This is because the thickness of most dikes in Santorini is less than 1 m, which is also close to the average thickness of 1.1 m (Drymoni et al., 2020). (Notice that since the thickness distribution is negative exponential it follows that the average thickness is much larger than the median thickness.) Thus, a 1 m thick dike with an aspect ratio of 1500 would have the strike-dimension of 1.5 km, which is much shorter than the estimated depth to the source chamber of about 4 km (Fig. 33). The strike-dimension is therefore smaller than the dip-dimension and therefore the controlling dimension. Thus, in Eq. (13) the symbol L would come in as the strike-dimension.

Using typical in-situ Young's modulus and Poisson's ratio values of young volcanic rocks at shallow depths, we have E = 10 MPa and ν = 0.25 (Gudmundsson, 2011). Using the large aspect ratio of 1500, as a starting example, Eq. (13) would yield a dike overpressure of about 3.6 MPa – which falls within the overpressure range for dikes as estimated by Kusumoto et al. (2013) and Biswas et al. (2023). At the shallow depth of the dikes exposed in the rims of the caldera (Figs 28 and 32), however, the aspect ratio may be somewhat lower. For example, at the very shallow depth of exposures of basaltic dikes in the active volcanoes of El Hierro (Canary Islands) the aspect ratio is only 171. Thus if we consider an aspect ratio of 300 as a low value for Santorini – which is also the lowest aspect ratio for measured dikes in Iceland (Gudmundsson, 2020) - then, from Eq. (13) and with the same values for the elastic constants as above, the dike overpressure would be 18 MPa. While rather high, this is still a plausible value, as indicated from numerous aspect ratio overpressure calculations worldwide (Becerril et al., 2013; Gudmundsson, 2020; Masoud, 2020).

Let us now consider the effect of magmatic overpressure in a dike in Santorini on the existing local stress gradient. For a dike to form there must be stress difference (anisotropic state of stress) at the potential site of the dike injection, either related directly to plate-tectonic forces or to excess pressure in a magma chamber and associated inflation, or both (Gudmundssson, 2020). This means that there exists a local stress gradient in the region of potential dike emplacement and the principal stresses are unequal (Figs 6, 9, and 10-15). More specifically,

for dike emplacement σ_1 is generally vertical and its magnitude with a larger (absolute) value than that of σ_3, which is then normally horizontal.

Stress effects of dike emplacement

Consider now a few scenarios as to how dike emplacement reduces the stress difference, and thereby the stress gradient (makes the local stress field more close to isotropic). When σ_1 is the vertical stress, as is normal for dike injection, then σ_1 is given, as a function of depth *z*, by the following equation (Gudmundsson, 2011):

$$\sigma_1 = \sigma_v = \int_0^z \rho_r(z) g dz \tag{14}$$

where *g* is the acceleration due to gravity (9.81 m s^{-2}), and $\rho_r(z)$ is the density of the rock layers as a function of depth. If the density of each layer is known, then Eq. (14) can be used to obtain the vertical stress at a given depth *z*. When the detailed density distribution of the rock layers is unknown, as is common, then the average density of the crustal rocks can be used, in which case (Eq. 14) reduces to:

$$\sigma_1 = \rho_r g z \tag{15}$$

where ρ_r is then the average density of the crustal rock column to a depth of z below the surface.

In the absence of direct measurements, σ_3 can be estimated in various ways. For a dike-emplacement stress field, the minimum horizontal stress σ_h would be σ_3, and we could use the following estimate (Gudmundsson, 2011):

$$\sigma_3 = \sigma_h = \frac{\nu \sigma_1}{1-\nu} = \frac{\sigma_1}{m-1} \tag{16}$$

where ν is Poisson's ratio and *m* is the reciprocal of ν (m = $1/\nu$) and is referred to as Poisson's number. A somewhat more sophisticated version of Eq. (16) is given by Fyfe et al. (1978), namely:

$$\sigma_3 = \frac{\sigma_1}{m-1} \pm \varepsilon_3 E \tag{17}$$

where, again, it is assumed that σ_1 is the vertical stress and σ_3 is the minimum horizontal stress. Here the horizontal strain (ε_3) is regarded as non-zero, but was assumed zero in Eq. (16). However, when the horizontal strain (positive if compressive and negative if tensile) is

not known, as is commonly the case, Eq. (16) can be used as a crude first approximation, as we shall do here.

The subaerial cliffs of the caldera rim of Santorini reach up to 300 m above sea level, but their maximum elevation where most of the dikes are exposed is commonly about 200 m. Similarly, the caldera floor, which is composed of four basins, reaches depths of 290-390 m below sea level (Perissoratis, 1995). It follows that a dike at 200 m depth below the surface of the caldera rim can theoretically be seen in the sea cliffs that constitute the caldera fault where most of the dikes are exposed (Figs 28 and 32). A typical young pile of lavas and pyroclastic layers, such as in Santorini, would have an in-situ average density similar to that typical of active rift zone or around 2300 kg m^{-3} (Gudmundsson, 1988). (Notice – this is the in-situ (field) density; the density of small laboratory specimens, free of fractures, cavities, and contacts, is normally much higher; Gudmundsson, 2020.) It then follows from Eq. (15) that at 200 m depth in the crust, we have σ_1 = 4.5 MPa. Using Eq. (16) with ν = 0.25 and, thus, m = 4, the minimum principal compressive stress is σ_3 = 1.5 MPa, so that we get the stress difference $\sigma_1 - \sigma_3$ = 3 MPa. It follows from the high-aspect ratio dike calculations above, where the estimated overpressure is about 3.6 MPa, that such a dike would neutralise the stress difference $\sigma_1 - \sigma_3$ in its vicinity and thereby make the stress field close to isotropic (and diminish the local stress gradient).

The stress effects of the dike intrusion fall off with distance from the dike (Fig. 19) but there are likely to be significant reduction in the stress difference and the stress gradient out to a distance of at least half the strike-dimension of the dike (Gudmundsson, 2011). In fact, significant temporary 'excess spreading rates' are detected through geodetic measurements many tens of kilometres away from regional dikes (Björnsson, 1985; Sigmundsson et al., 2015) – as expected from the results of numerical modelling of dikes (Gudmundsson et al., 2014; Bazargan and Gudmundsson, 2019). What the results show, however, is that even with a comparatively low overpressure, a dike intrusion would tend to move the local stress field towards an isotropic field and thereby reduce stress differences and stress gradients.

When considering deeper crustal levels, such as 1 km, then the in-situ crustal density used must be higher. A common average density for the uppermost 1 km of the crust is about 2500 kg m^{-3} (e.g., Gudmundsson, 1988, 2020). Then from Eq. (15) the vertical stress σ_1 at 1 km depth would be 24 MPa and the minimum horizontal compressive stress, from Eq. (16), about 8 MPa. The stress difference is thus $\sigma_1 - \sigma_3$ = 16 MPa. In this case the overpressure associated with the smaller aspect ratio, namely the overpressure of 18 MPa, would approximately neutralise the stress difference and bring the local stress field, following dike emplacement, close to isotropic.

There are several aspects to consider when applying Eqs (15) and (16) to estimate the local stress field before dike injection. The first is that large stress differences, such as implied by σ_3 being 1/3 σ_1, cannot exist at and close to fluid magma sources - in Santorini this would be the shallow magma chamber (Browning et al., 2015). This follows because when the chamber

is neither expanding nor contracting, as is the situation most of the time, the total fluid pressure inside the chamber (Eq. 11) is in equilibrium with the external stress, which is then normally isotropic (and lithostatic) in which case we have:

$$\sigma_1 = \sigma_2 = \sigma_3 = p_1 \quad (18)$$

where p_l is the lithostatic stress or overburden pressure. Eq. (11) indicates that as soon as σ_3 in the roof of the chamber, that is, at its boundary with the magma, is reduced by a stress equal to the tensile strength T_0 of the host rock at that boundary, a dike (or an inclined sheet, depending on the local stress field) is injected. This reduction in σ_3 can be reached through increase in magmatic pressure in the chamber by p_e (Eq. 11), or by horizontal tectonic extension (due to plate movements or local spreading in the volcano), or both. Since all the principal stresses are initially the same (Eq. 18), the maximum difference between the principal stresses that can occur before a dike is injected and reduces the stress difference is:

$$\sigma_1 - \sigma_3 = T_0 \quad (19)$$

Given that the tensile strength is commonly only 2-4 MPa, with a maximum measured value of about 9 MPa (Gudmundsson, 2011), it follows that the maximum stress difference at the boundary with the chamber before dike injection is 9 MPa and more commonly 2-4 MPa. Thus, it is not possible for the chamber boundary, the roof next to the chamber, to reduce σ_3 to the value given by Eq. (16), namely 1/3 σ_1. Long before that could happen, a dike injection would restore the stress difference to essentially zero, so that the state of stress at and close to the boundary of the chamber would again be isotropic and as given by Eq. (18).

The second aspect to be considered is that very close to the surface, particularly where there is active plate-tectonic spreading, σ_3 may become negative. The meaning here is not dike-induced tensile stress which can reduce σ_3 so much as to make it negative (Bazargan and Gudmundsson, 2019, 2020). It is rather that σ_3 may in some places become negative (irrespective of dike or inclined sheet injection) as a direct consequence of the tensile force associated with plate-tectonic movements. Tensile stresses close to and at the surface may generate tectonic tension fractures (Fig. 27). Such fractures are not common in Santorini, but they are very common at divergent plate boundaries, such as in Iceland, to which we turn in the next section.

What the above results show, however, is that dike injection tends to bring the state of stress close to isotropic, thereby reducing stress differences and stress gradients. If the dike overpressure is high, then the principal stresses may swap so that, for a while, σ_1 becomes horizontal in a direction perpendicular to the dike. But in all tectonically active areas, excess dike-induced horizontal stresses gradually relax so that, again, the state of stress becomes closer to an isotropic one. It may stay as such for a while but in areas of active

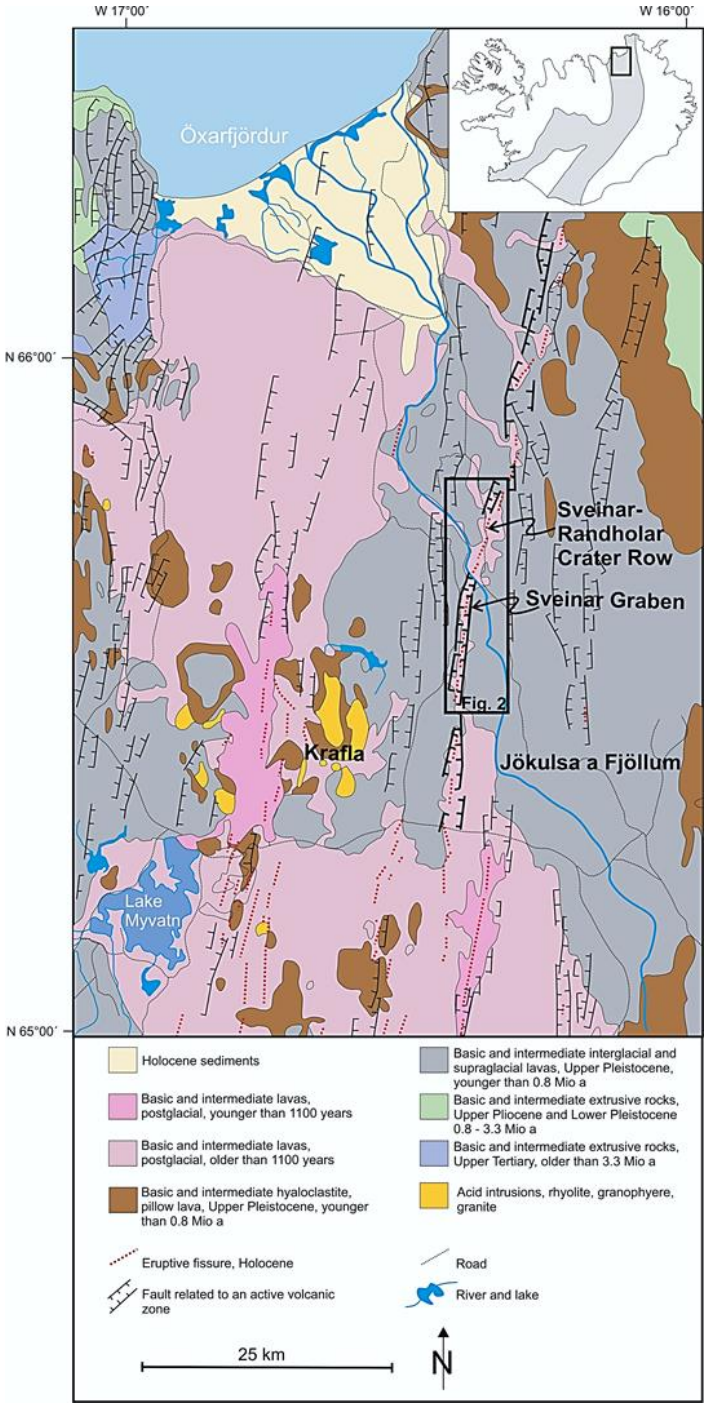

Fig. 34. Location of the reverse fault and the dike causing the reverse slip as seen it in Fig. 35 and modelled in Fig. 36 (also located on the inset map of Iceland; the indicated fig. 2 is omitted here). They are both located within the Sveinar graben and the dike supplied magma to the Holocene Sveinar-Randarholar crater row (Gudmundsson et al., 2008).

volcanotectonic processes, the stress again may become anisotropic so as to build up anew a stress gradient that favours dike/inclined sheet injection, faulting, or both.

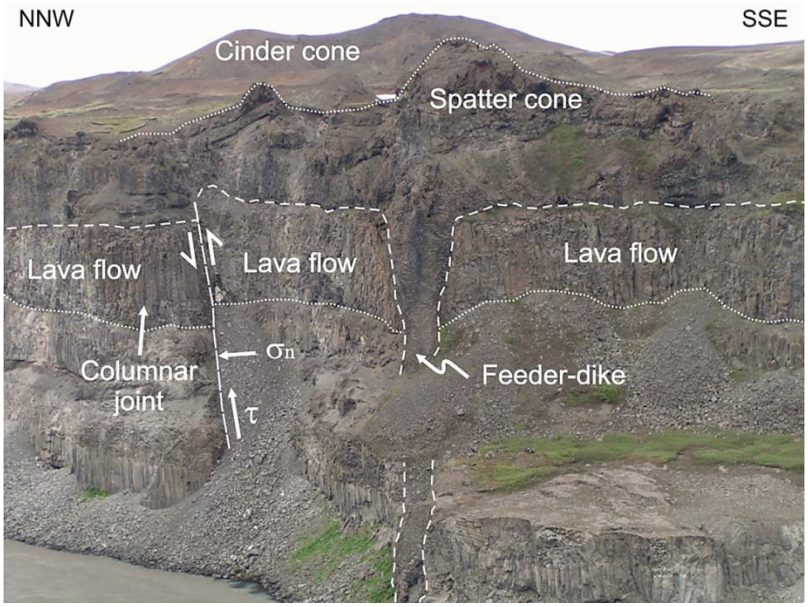

Fig. 35. View north across the river (Jökulsa a Fjöllum, Fig. 34) to the eastern canyon wall showing the eastern feeder-dike segment to the Sveinar-Randarholar crater row being connected to one of its spatter cones. The thickness of the exposed feeder-dike ranges from 4.5 m at the bottom of the canyon to 13 m where the dike is connected with the spatter cone. The reverse fault is indicated by white arrows – as are the normal stress σ_n acting against the displacement and driving shear stress τ causing the reverse displacement. The fault has a reverse displacement of about 5 m, some 40 m from the centre of the dike inducing the reverse movement on an otherwise normal boundary fault of the Sveinar graben. The host rock is primarily composed of interglacial basaltic lava flows (Gudmundsson et al., 2008).

Faulting in Iceland

Both dip-slip and strike-slip faulting is common in Iceland. Many of the strike-slip faults are conjugate, as described below. Small strike-slip faults occur everywhere, but the larger ones are primarily confined to two transform zones, one in the northern and the other in the southern part of the country (Fig. 16). Dip-slip faults comprise normal faults and reverse faults, the latter being classified as thrust faults when the dip is less than 45°. Given that Iceland is the site of a divergent plate boundary with three main volcanic zones where rifting is taking place (Fig. 16 – rifting is very limited in the off-rift Snaefellsnes Volcanic Zone), normal faults are the most common types of faults. However, there are also numerous tectonic tension fractures in the volcanic rift zones of Iceland (Fig. 27). There are, additionally, some reverse faults in Iceland. While these are understandably fewer than the normal faults, the reverse faults throw an interesting light on the process by which a local stress field in an active area may be shifted in the direction of a temporary isotropic state of stress. We therefore begin the discussion of the effect of faulting in reducing stress gradients by considering an exceptionally well-exposed reverse fault.

Reverse faulting

A boundary fault of a graben, and thus initially a normal fault, has been changed into a reverse fault through the horizontal compressive stress induced by a feeder-dike in North

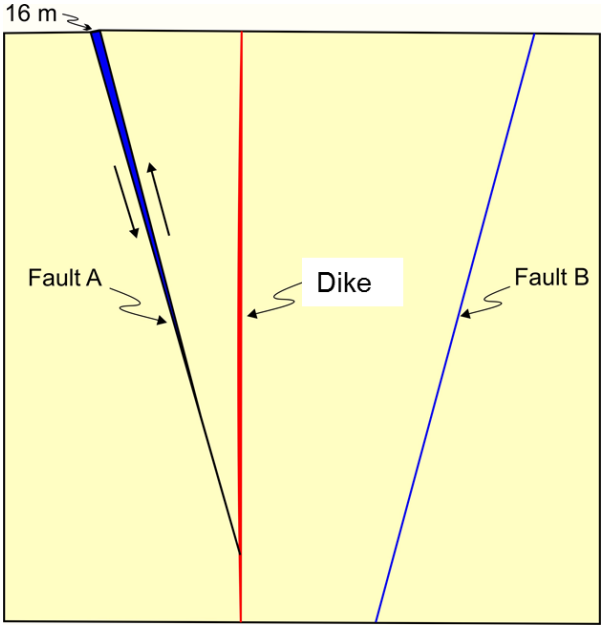

Fig. 36. Numerical model of the effects of the dike with an estimated magmatic overpressure of 10 MPa on the graben boundary (initially normal) faults A and B (Gudmundsson et al., 2008). Fault A is the one seen in Fig. 35 but fault B is outside the section shown in Fig. 35. In the model, the faults extend from the free surface to a depth of ~100 m (the bottom of the canyon, Fig. 35). The feeder-dike emplacement has hardly any effect on fault B, but causes reverse slip by as much as 15-16 m on fault A. Since fault A was initially with a normal-fault displacement of about 10-11 m, the induced reverse slip has resulted in its present displacement being about 5 m reverse – so that the modelling results fit broadly with the measurement results.

Iceland (Fig. 34). Away from the feeder-dike, the graben has normal faults with displacements anywhere between (commonly) 2-7 m and 22 m. One of the boundary faults in the east wall of the canyon is only 40 m from the feeder-dike (Fig. 35), whereas the other boundary fault is 80 m from the feeder-dike (and not seen in Fig. 35 but indicated in Fig. 36). The fault at a distance of 80 m is still a normal fault, whereas the fault at 40 m from the feeder-dike has changed from a normal fault to a reverse fault with a measured reverse displacement of 5 m.

Earlier numerical models show that dike injection into a graben may cause reverse slip on the normal boundary fault of the graben (Gudmundsson and Loetveit, 2005). In these early models the dike propagated up through the central part of (bisected) the graben. For this particular case in North Iceland, the feeder-dike is much closer to the west boundary fault than to the east boundary fault (Figs. 35 and 36), so, as stated, the effect of the injected dike is only seen on the east boundary fault.

For a numerical model on the likely displacement on the boundary fault for the present dike (Fig. 36), Gudmundsson et al. (2008) applied the following boundary conditions. First, using Eq. (11) the regional dike overpressure was estimated as ranging from 4 to 21 MPa, with a common value of about 10 MPa. Since the dike is very close to the surface, this overpressure translates into a horizontal principal compressive stress, that is, horizontal σ_1 of 10 MPa. These overpressure values are similar to those obtained in the last section for the dikes in

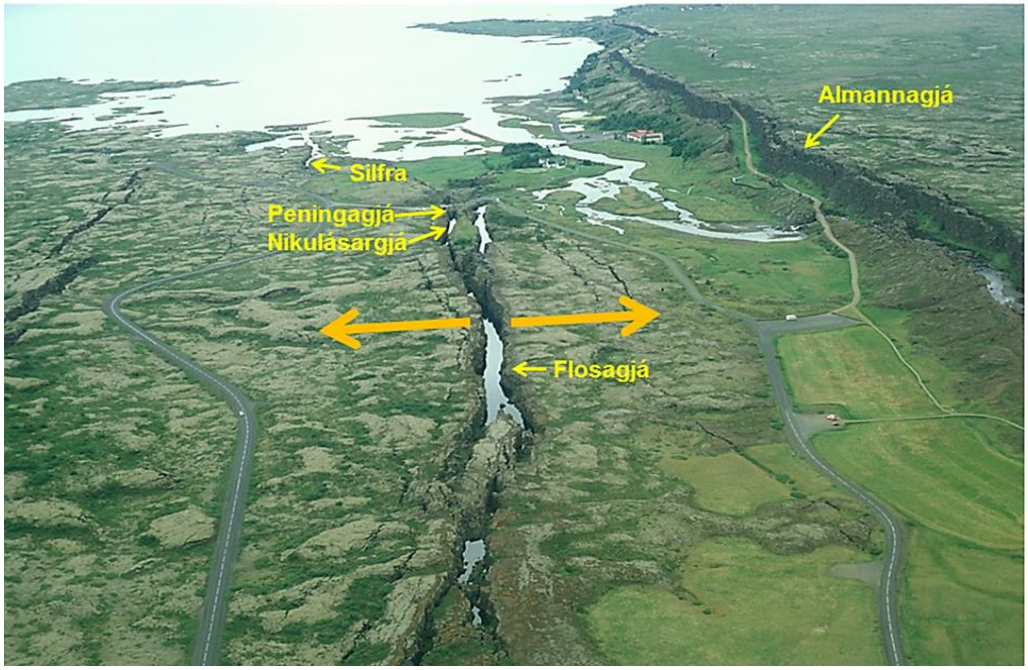

Fig. 37. Aerial view southwest along part of the West Volcanic Zone (located in Fig. 16) showing large-scale tectonic tension fractures and normal faults. More specifically, the named tension fractures Peningagjá and Nikulásargjá (cf. Fig. 27) are a part of the main fracture Flosagjá. Also shown is the tension fracture Silfra and the large normal fault Almannagjá (whose cross-section is seen in Fig. 39). The plate-tectonic forces (associated with the spreading vectors in Fig. 16) generating the tension fractures and normal faults are indicated schematically by orange arrows at Flosagjá (cf. Gudmundsson, 2017).

Santorini. Using the measured attitude (strike and dip) of the boundary faults (the dip of fault A, the reverse fault, is 75°E) and a typical Young's modulus of 10 GPa and a Poisson's ratio of 0.25 (same values as used above for the Santorini calculations), the calculated reverse slip on fault A is 16 m (Fig. 36). Because the present reverse slip on fault A (Figs 35 and 36) is 5 m, then the original normal-fault displacement of the fault, before the reverse slip induced by the feeder-dike, was 10-11 m – a result that is very plausible given the normal-fault displacement on the graben boundary faults far away from (and thus not affected by) the feeder-dike.

The horizontal σ_1 at and close to the surface gives rise to a stress gradient, that is, stress difference of $\sigma_1 - \sigma_3$ = 10 MPa. This follows because at the surface σ_3, which is vertical for reverse faulting, is just the atmospheric pressure, which is 0.1 MPa (1 bar) and may thus, for the present purpose, be regarded as zero. How does the faulting then bring this stress difference again close to zero so as to reduce the gradient?

The reverse slip effectively means that there is horizontal shortening of the crustal segment, the exposed lava flows as seen in the canyon (Fig. 35) – although the shortening extends to greater depths (Fig. 36) – which means that the applied horizontal σ_1 due to the overpressure of the dike becomes reduced, presumably effectively to zero at the surface, thereby bringing the state of stress again closer to isotropic (and minimising the stress gradient). The reverse

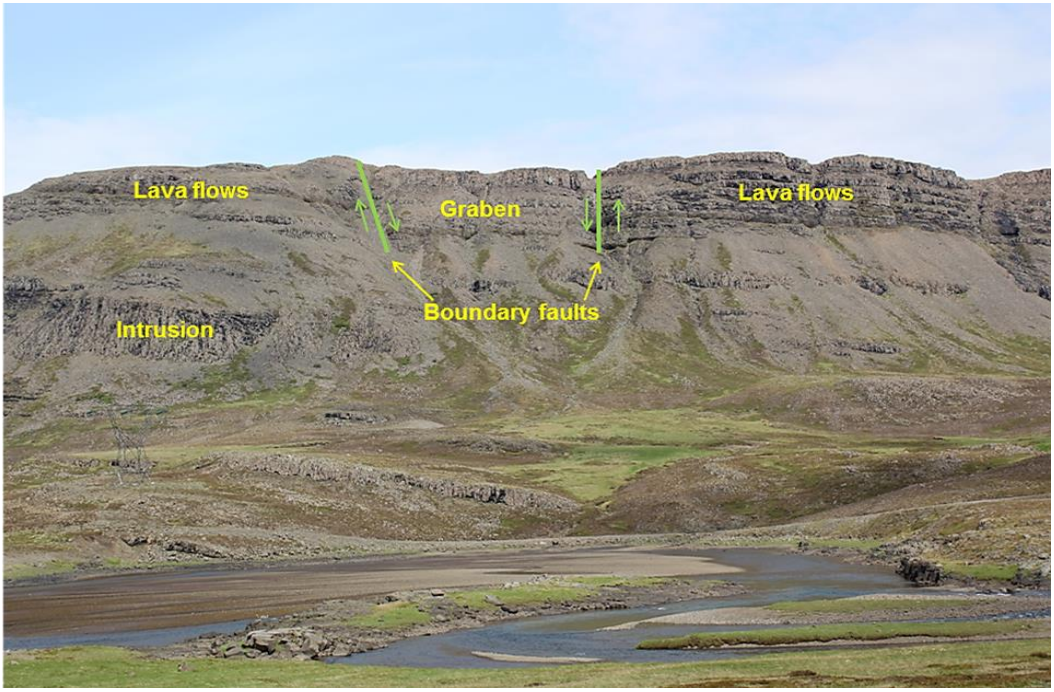

Fig. 38. Two normal boundary faults dipping towards each other constitute a graben (cf. Figs 21, 26, and 31), as seen here in the lava pile of Southwest Iceland (cf. Gudmundsson, 2017). The mountain is primarily composed of basaltic lava flows, with some intrusion, primarily sills (a thick intrusion is indicated) and dikes. The overall vertical displacement (subsidence) of the graben is about 30 metres, which is similar to that measured of Almannagjá normal fault in the nearby West Volcanic Zone (Figs 37 and 39).

fault displacement is also one reason why the feeder-dike is so thick at the surface (at time of dike formation and eruption some 8000 years ago) where it connects with the spatter cone to which it supplied magma. At the bottom of the canyon the feeder-dike is just over 4 m thick, but at its connection with the spatter cone (namely at the surface at the time of eruption) the dike thickness is about 13 m. Some feeder-dikes become thinner close to the surface (Galindo and Gudmundsson, 2012; Corti et al., 2023), whereas other feeder-dikes become thicker at the surface (Geshi et al., 2012).

Some feeder-dikes become much thicker very close to and at the surface because there they dissect compliant scoria layers of much lower Young's modulus than that of the stiffer lava flows below (Geshi and Neri, 2014). For the present feeder-dike, the increase in thickness (palaeoaperture), that is, in opening displacement close to the surface, is presumably partly related to the existing fault and its easy displacement close to the surface. Fractures of all kind lower the effective Young's modulus (Gudmundsson, 2011), and so do faults that slip easily.

Normal faulting

Normal faults are very common in the volcanic rift zones of Iceland (Fig. 34) – and also in the palaeorift zones (Fig. 26). In the active rift zones, there are specific swarms of normal

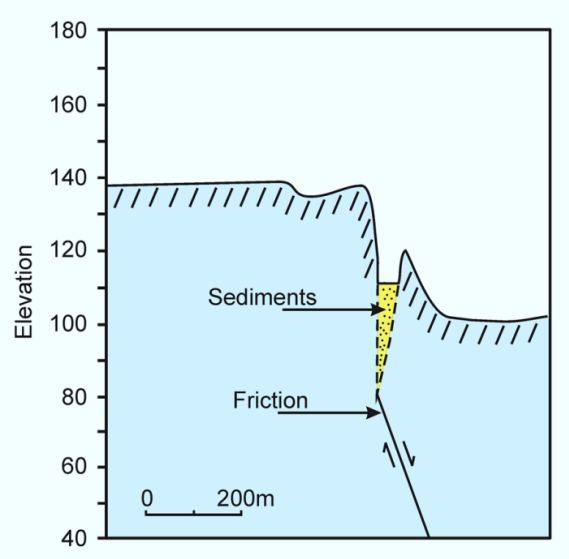

Fig. 39. Schematic cross-section through the central part of the normal fault Almannagjá (the section is close to the location of the word Almannagjá in Fig. 37). The western (left) fault wall reaches about 140 m above sea level, whereas the lowest surface on the eastern (right) wall is at about 100 m above sea level, so that the maximum vertical displacement on the fault is here about 40 metres. As the fault walls meet at depth, the friction causes tilting of the east wall so that the fault dip to change from vertical (originally a tension fracture) to a steeply dipping fault. As drawn the vertical scale is exaggerated about 8-times the horizontal scale (modified from Gudmundsson, 2017).

faults and tension fractures (Figs 27, 37, 38, and 39). Both the opening of tension fractures and the slip on normal faults seek to reduce the stress difference $\sigma_1 - \sigma_3$ so as to make the stress, for a while, closer to isotropic. As regards the tension fractures, the reduction in the stress occurs only close to the surface. This is because tectonic tension fractures of the type seen in rift zones are rarely deeper than a few hundred metres and many much shallower (Gudmundsson, 2011, 2020). Thus, at the surface, a tectonic tension fractures normally forms because σ_3 is negative (and parallel with the local plate-tectonic spreading vector – Fig. 37) and equal in magnitude to the tensile strength of the rock at the time of fracture formation. Thus, formation of a new tension fracture, or further opening and lengthening of an existing one, results in relaxation of the magnitude (absolute value) of σ_3, bringing it close to zero. Since the vertical stress σ_1 is also close to zero (atmospheric pressure) at the surface, this reduction in the magnitude of σ_3 means that $\sigma_1 - \sigma_3$ approaches zero and the state of stress becomes close to isotropic. Thus, tension fracture formation or reactivation tends to bring about, temporarily, isotropic state of stress at shallow depths, that is, to diminish any tensile stress gradients.

At depths greater than a few hundred metres, however, the reduction in $\sigma_1 - \sigma_3$ in areas of rifting is, in volcanic areas, primarily reached through dike injection and normal faulting. In areas of extension where dike injection is largely absent, such as in many sedimentary basins, the reduction in the stress difference $\sigma_1 - \sigma_3$ is primarily through normal faulting. Here we focus on field examples of normal faulting from Iceland.

The stress-effect of normal faulting is perhaps easiest to visualise when considering grabens (Figs 26, 31, and 38). Initially, before normal faulting, or before further slip on the normal faults if they already exist, the state of stress is as indicated in Fig. 30a. Thus, as for tension fractures, σ_1 is vertical and σ_3 is horizontal and perpendicular to the strike of the normal faults/graben. When displacement occurs on the normal faults, their movement (primarily) down the fault plane increases the (compressive) magnitude of σ_3 - as, for a graben, the wedge-shaped crustal segment between the boundary faults subsides into a narrower space and generates horizontal compressive stress – thereby making the stress difference $\sigma_1 - \sigma_3$ approach zero. The normal-fault movement, therefore, brings the local stress field closer to that of an isotropic field, thereby reducing the stress gradient.

Some normal faults in rift zones gradate into open or gaping fractures at the surface (Figs 37 and 39). This occurs primarily in stiff layers such as lava flows. This is because lava flows have a non-zero tensile strength, commonly 2-4 MPa, so that they can build up absolute tension and host tension fractures. Many of the faults, in fact, develop from tectonic tension fractures which must change into normal faults on reaching a certain depth – normally depths of the order of a few hundred metres. By contrast, normal faults maintain their dips up to the surface, that is, do not change into tension fractures, where they dissect young compliant surface layers with essentially no tensile strength. This is commonly the case where normal faults dissect layers of young sediments (such as sea or lake sediments, as are common in Iceland), as well as when faults dissect young hyaloclastites (Gudmundsson, 2011).

Strike-slip faulting

Small-scale strike-slip faulting occurs throughout Iceland (Bergerat, 2021; Bergerat et al., 1990, 1998, 2003; Villemin et al., 1994; Gudmundsson, 2017; Gudmundsson et al., 1992, 1996). This has been determined from slickenside studies (Bergerat et al., 1990, 1998, 2003; Bergerat, 2021). Much of this strike-slip faulting is induced by dike emplacement. As indicated above, the overpressure of a propagating dike is transformed into the host-rock walls at the contact with the dike as horizontal compressive stress. The resulting faulting may be partly reverse, as discussed above, and partly strike-slip faulting. Normal faulting would be primarily expected above the upper tip of the dike – in and above its process zone (Gudmundsson, 2020). All these types of faulting have been reported through focal mechanism in recent dike-injection events in Iceland (e.g. Agustsdottir et al., 2015).

Large-scale strike-slip faulting is, however, primarily confined to two seismic zones, one in North Iceland, the other in South Iceland (Fig. 16). The one in the north is the Husavik-Flatey Fault (HFF), a 90-km-long and 5 km wide (graben structure) transform fault that is partly exposed on land and connects the mid-ocean Kolbeinsey Ridge with the rift zone in North Iceland. The other one is the South Iceland Seismic Zone (SISZ) which is a sort of transform zone that connects the East Volcanic Zone with the West Volcanic Zone and its continuation along the Reykjanes Peninsula (Gudmundsson and Homberg, 1999). In contrast with the

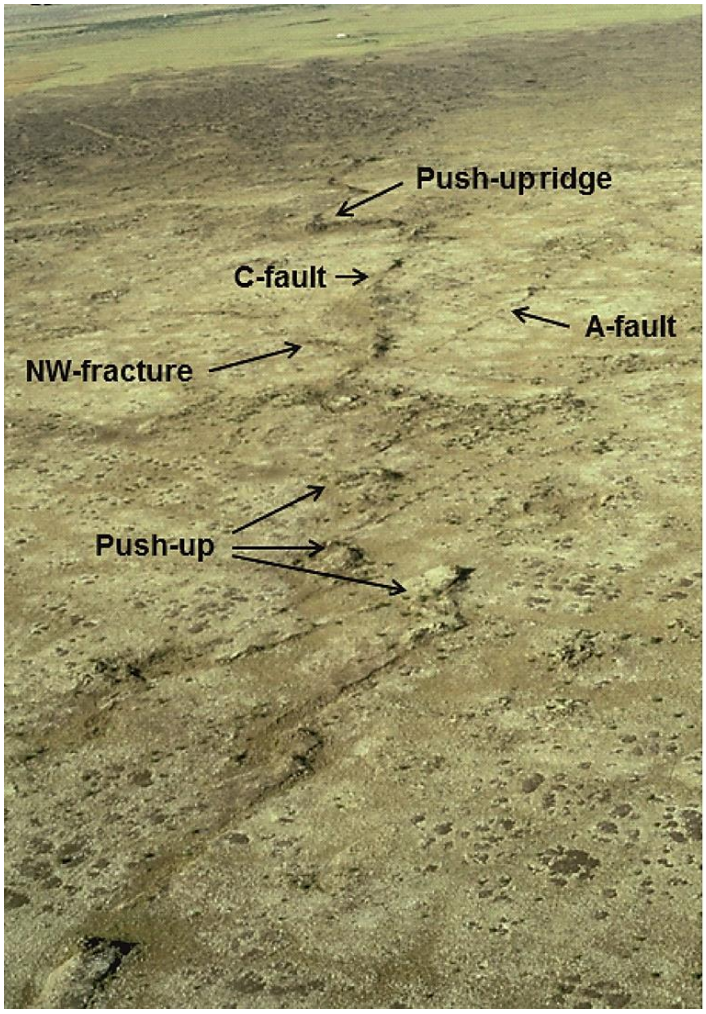

Fig. 40. Aerial view north of a strike-slip fault in the South Iceland Seismic Zone (cf. Fig. 16 and Gudmundsson, 2017). Strike-slip faults such as this one (here dissecting a Holocene basaltic lava flow) are characterised by hillocks and ridges referred to as push-ups. The main fault, a north-striking dextral fault (denoted as C-fault), and a smaller northeast-striking sinistral fault (denoted as A-fault) form conjugate faults. Additionally, there is a northwest-striking fracture associated with the fault pattern.

HFF, the SISZ is not a clear transform fault at all; it has no major E-W striking fault. It is rather a zone of numerous, mainly, NNE-striking and ENE-striking strike-slip faults, with some additional fracture strikes. The SISZ offers the best example in Iceland of strike-slip faulting contributing to reduction in the stress difference $\sigma_1 - \sigma_3$ so we shall use them as examples here.

Some of the strike-slip faults in the SISZ are tens of kilometres long (Fig. 40). They give rise to earthquakes that in recent decades have reached M6.6 while the largest ones may reach at least M7.1 (Jakobsdottir, 2008; Gudmundsson, 2017). The main faults are conjugate where the NNE-striking faults are dextral and the ENE-striking faults are sinistral (Figs 40 and 41). The maximum slips on the faults during earthquakes in recent decades have been 1-2 m, but on some of the largest faults that have been active in the past centuries the slips reach 2-3 m

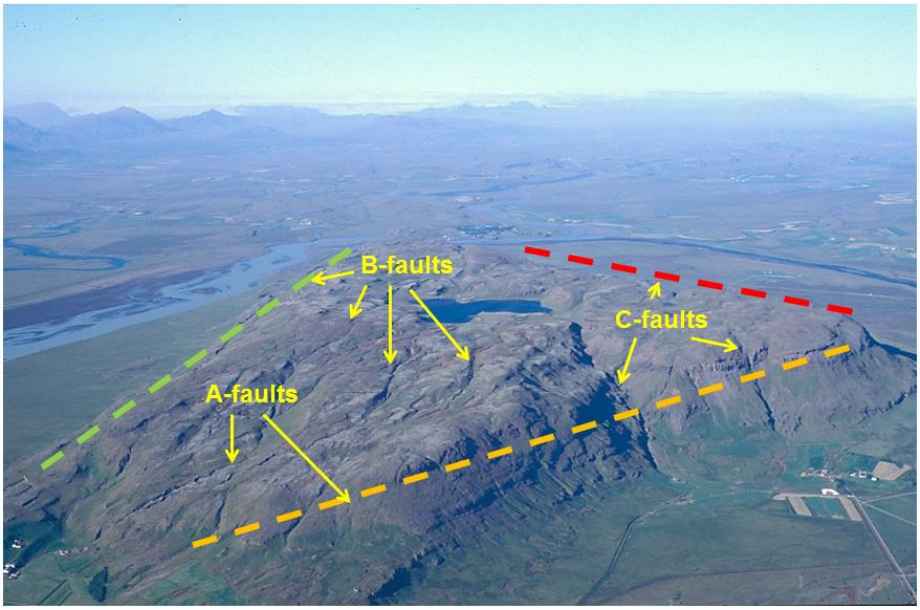

Fig. 41. Aerial view northeast of strike-slip and normal faults dissecting the hyaloclastite mountain Vördufell – the strike-slip faults being related to the South Iceland Seismic Zone (cf. Figs 16 and 40 and Gudmundsson, 2017). The slopes of the mountain coincides crudely with the three main fault strike and give the mountain its triangular shape. These are: east-northeast striking sinistral strike-slip faults (denoted as A-faults), northeast-striking normal faults (denoted as B-faults), and north-striking dextral strike-slip faults (denoted as C-faults).

(Bergerat et al., 2003). The maximum cumulative displacements on strike-slip faults in South Iceland, however, 15 m (Gudmundsson and Homberg, 1999).

From Fig. 30 it follows that slip on conjugate faults results in shortening in the direction of the horizontal σ_1 and thereby reduces the magnitude of σ_1. At the same time, the slip results in horizontal expansion of the crustal segment in the direction of σ_3, thereby increasing its (compressive) magnitude. The overall result of slip on conjugate strike slip faults is thus to reduce the stress difference $\sigma_1 - \sigma_3$, thereby diminish any stress gradients and bring the local state of stress closer to isotropic.

Discussion

During loading, any rock body within the brittle crust with mechanical properties that differ from those of the surrounding rock (host rock) modifies the local stress field. If the considered body is a hole or cavity filled with some fluid (e.g., air, water, or magma) the local stresses will concentrate, that is, be raised, around the body (Figs 1 and 2). If the body under consideration is solid, then, depending on its properties, the local stresses around that part may either become raised (concentrated) or lowered (suppressed). If the solid body has a lower Young's modulus than that host rock, it can be modelled as a soft elastic inclusion

(Figs 4 and 25) which tends to suppress the stresses inside the body and in its close vicinity. If the solid part has a higher Young's modulus than the host rock (Figs 3 and 5), however, then the body acts as a stiff elastic inclusion which tends to raise the stresses at its margins and in their close vicinity.

Stress modifications resulting in increase or decrease in the magnitude of crustal stresses at a given locality generate stress gradients. A stress gradient is just one among many other gradients in nature. These include geothermal gradients, chemical pollution (e.g. air or water pollution) gradients, hydraulic gradients (which control the transport of groundwater), air pressure gradients, and topographic (landscape) gradients. The gradient is a vector (Eq. 2) whose direction at a given point is that in which the function that defines the scalar field under consideration (e.g., temperature, pressure, or elevation above sea level) – here denoted by ϕ - increases most rapidly. Furthermore, the magnitude or size of the gradient is the rate of increase of ϕ in that direction.

The transport or 'flow' (such as of groundwater or heat) is always down the gradient, that is, from higher to lower values (for example, of temperature, elevation, pressure, energy, and concentration of polluting materials). This means that the transport is in the direction of the negative of the gradient, that is, in the direction of $-\nabla\phi$ (Eq. 2). As applied here to crustal stress fields, gradients arise because the stresses at certain locations – in certain parts of the crust, such as at and around rock bodies (e.g., Figs. 3-5 and 22-23) – are different (higher or lower) from those in the surrounding parts of the crust, that is, in the host rock.

The results presented here show, analytically and numerically, that stresses concentrate around totally and partially fluid magma chambers when they are subject to loading (Figs 6-15). This means that the stresses are magnified, are raised, at the margin of, and in the close vicinity of, the magma chambers when subject to loading that is internal (excess magmatic pressure), external (tensile stress), or both. For solid rock bodies, such as intrusions/plutons (Figs. 3, 5, and 26), and active or fossil fault zones (Figs 4 and 22-25), the stresses may either increase or decrease inside and in the close vicinity of the body. All these bodies function essentially as elastic inclusions (Fig. 4), either as stiff inclusions (if Young's modulus of the body is higher than that of its host rock) or soft inclusions (if Young's modulus of the body is lower than that of its host rock). When the rock body acts as a stiff inclusion, stresses concentrate inside and in the close vicinity of the body. When, however, the body acts as a soft inclusion, as is common for active fault zones with well-developed cores and damage zones (Figs 23-25), the stress concentration (raised stress) is transferred to the outer parts of the damage zone and into the host rock (Fig. 25; Gudmundsson et al., 2010). This is partly the way that active fault zones gradually increase their thickness (Gudmundsson, 2011), while the central part of the fault zone continues to be mechanically its weakest part (with the lowest shear strength) and thus subject to frequent slips.

Here I propose that stress gradients in the brittle part of the crust are, in volcanically and/or tectonically active areas, gradually reduced through brittle deformation. The main outcrop-

scale deformation in such areas occurs through dike/sheet emplacement, faulting (and tension-fracture formation at shallow depth), or both. Close to active magma chambers, the associated stress gradients (Figs 5-15) – primarily tensile stress – are gradually reduced through dike/sheet injection, that is, extension fractures (Figs 26, 27, 28 and 32). Thus, dike/sheet injections repeatedly alter the local stress field around a magma chamber so as to bring it close to istropic, that is, to lithostatic state of stress. Once the stress state is back to lithostatic, the chamber remains in lithostatic equilibrium with the host rock, and no further dike injections or faulting takes place until the state of stress is again – through external and/or internal loading - favourable for dike/sheet injection (Eq. 11).

So long as a chamber is within a tectonically active area or zone, which normally means that the chamber (and the volcano it feeds) is associated with a plate boundary or a mantle plume (or both, such as in Iceland), the stress around the chamber gradually concentrates again following dike/sheet injections. This means that while the plate-boundary loading on the magma chamber continues, then after each dike/sheet injection and reduction in the stress gradient (resulting in approximately lithostatic stress state) stress at the margin and in the close vicinity of the chamber increases again until the conditions of Eq. (11) are satisfied and a new dike/sheet injection takes place. The injection temporarily changes the state of stress again to approximately lithostatic and, thereby, reduces the local stress gradient – and then the process repeats itself so long as the chamber is within a tectonically active zone.

The same applies to tectonic faulting. So long as the area or zone of faulting is subject to renewed loading – which, again, normally means that the zone is a part of, or close to, a plate boundary – then following faulting and reduction in stress gradients the local stresses build up again (and so does the stress gradient – it becomes steeper) until renewed faulting takes place, and the process repeats itself. The overall effect of faulting on the development of local stresses is somewhat different from the effect of dike/sheet intrusions. This is primarily because of the different effects which faulting, on one hand, and dike/sheet intrusion, on the other, have on the effective Young's modulus of the rocks that constitute the hosting crustal segments. When dikes/sheets solidify, they become stiff and commonly have higher Young's modulus than the host rock. They thus become stiff elastic inclusions (Figs 3, 5, 28, 32 and 35). By contrast, so long as a fault is active, its damage zone and core gradually increase in thickness (Figs 22, 23, and 24), the effective Young's modulus of the fault decreases (Gudmundsson, 2011), and the fault remains a soft elastic inclusion (Figs 4 and 25). This means that both for individual faults, and in larger areas or zones of active faulting, the effective Young's modulus gradually decreases over larger volumes. Thus, stresses due to continued loading are transferred into the outer parts of the damage zone and, eventually, into the host rock (Fig. 25). The thickness of a fault zone, or its volume in three-dimensions, thus gradually increases (Gudmundsson, 2011; Gudmundsson et al., 2010). However, the central part of the fault, the core and core-damage zone contact, remain a major slip zone because they are mechanically weaker than the surrounding rocks.

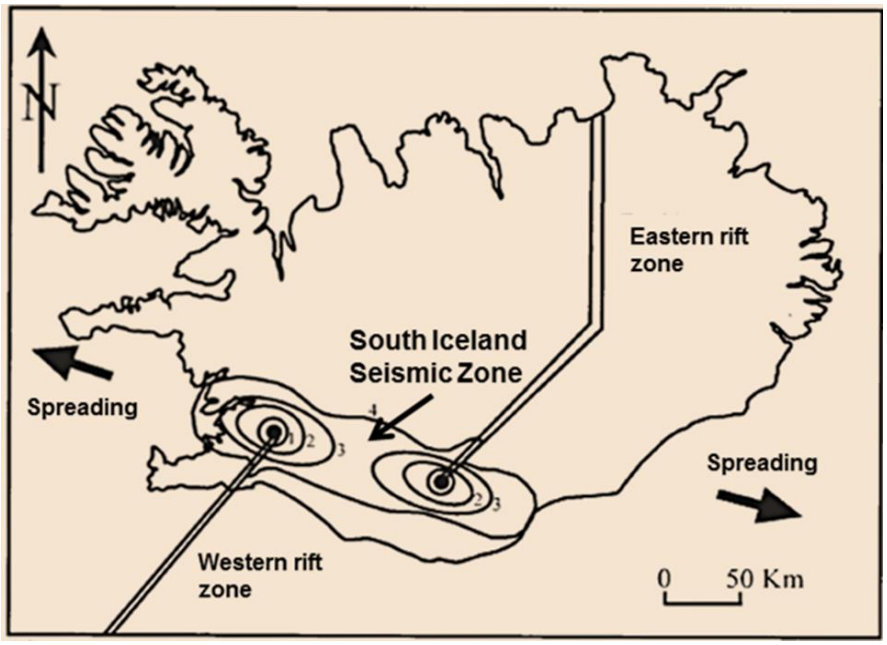

Fig. 42. Schematic model of the migration of shear stress conditions for fault slip and associated seismicity in the South Iceland Seismic Zone (SISZ). Following a large earthquake and stress relaxation, the seismicity is largely confined to one or both of the junctions between the seismic zone and the rift-zone segments. Build-up of tensile stress due to plate movements in the adjacent ridge segments, however, leads to gradual expansion of the conditions for fault slip throughout the seismic zone (Gudmundsson and Homberg, 1999).

We can illustrate the general transfer of stresses into the rocks hosting a seismically active fault zone or area by a simple model of the South Iceland Seismic Zone, SISZ (Fig. 42). Initially, the stresses concentration begins where the loading effects are greatest. This is commonly at some juncture in the geometry of the seismic zones (or where there are local changes in Young's modulus) - in Iceland at the intersection between seismic and volcanic zones. At the beginning of a 'seismic cycle', that is, following earthquakes that have relaxed much of the stress in the area or zone of faulting, the stresses begin to concentrate at location where the geometry and/or the rock properties favour concentration. Even if the effective in-situ Young's modulus gradually becomes lower, due to fracture formation, at the location of the geometrically favoured site for stress concentration, the main local source of stress for the fault zone remains there during the seismic cycle. The local stress source may be at only one site within the fault zone but, depending on the geometry of loading, it may also be at two or possibly more sites.

The SISZ is an example of a major seismic zone with two main stress sources (Fig. 42). In this schematic illustration, the stresses concentrate primarily at the intersection between the SISZ and the two main rift zones. Here the Eastern rift zone (which forms a part of the East and North Volcanic Zones, Fig. 16) ends in the southwest at its contact with the SISZ. This is because the part of the volcanic zone southwest of the SISZ is no longer a rift zone but a propagating rift (Gudmundsson, 2017). The Western rift zone is also simplified in that there is rifting north of its junction with the SISZ, but the main rifting is presumably south of the

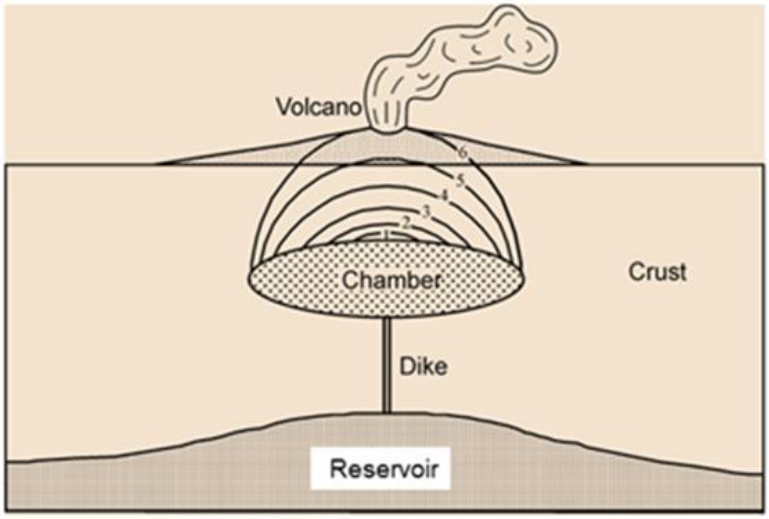

Fig. 43. Majority of dikes and inclined sheets injected from a shallow source magma chamber of a volcano become arrested in various crustal 'shells' or barriers (1–5) where the stresses, at a given time, are unfavourable to the propagation of these intrusions. This is partly because during unrest periods the tensile stress first concentrates around the chamber and reaches the conditions for dike/sheet injection at the chamber margins (mainly in its roof) often earlier in the unrest period than those conditions are reached further away from the chamber. Thus, the stress magnitudes decrease with distance from the chamber – as is very commonly observed for stress gradients (Figs 1, 6, 9, 10, 11, 13, 14, and 15). Gradually, however, as the chamber-induced stresses expand and the stress field becomes homogenised. Eventually, the stress conditions favourable to dike/sheet propagation may reach to the surface, encouraging dike/sheet-fed eruptions (6). Modified from Gudmundsson and Brenner (2005).

SISZ where the Western rift zone takes over from the Eastern rift zone as the main zone of rifting in Iceland (Gudmundsson and Homberg, 1999).

Based on this schematic presentation, and the plate-tectonic vector that provides the loading, the proposed evolution of the seismic cycle in the SISZ is as follows (Fig. 42). Following large earthquakes, there is stress relaxation in the zone. The largest earthquakes in the SISZ are thought to reach M7.1, but the largest in recent decades were the two M6.6 June 2000 earthquakes (Jakobsdottir, 2008; Gudmundsson, 2017). Following a general or partial stress relaxation, the stresses build up again in the seismic zone, first at the junctions between the rift zones and the SISZ (Fig. 42). There the stress conditions for fault slip are first (and most frequently) met. Because the stress-concentration areas at the early stages (contours 1-2) of the earthquake cycle are small, the conditions for fault slip are satisfied in comparatively small parts of the SISZ and none of the earthquakes reach above M3-4. The long-term fracturing in these regions, which have been subject to fracturing for tens of thousands of years or more (Gudmundsson, 2017), means that their effective Young's modulus is comparatively low, so as the plate-tectonic displacement across the SISZ and associated loading continues, stresses become partly transferred from regions 1-2 to larger (and less fractured, and thus with a higher effective Young's modulus) parts of the SISZ (contour 3), until, eventually, the entire zone is highly stressed (contour 4; Fig. 42). At this stage, large earthquakes can be expected in the SISZ. When these occur, the resulting stress relaxation brings the SISZ again to the stage where earthquake-generating stresses are essentially

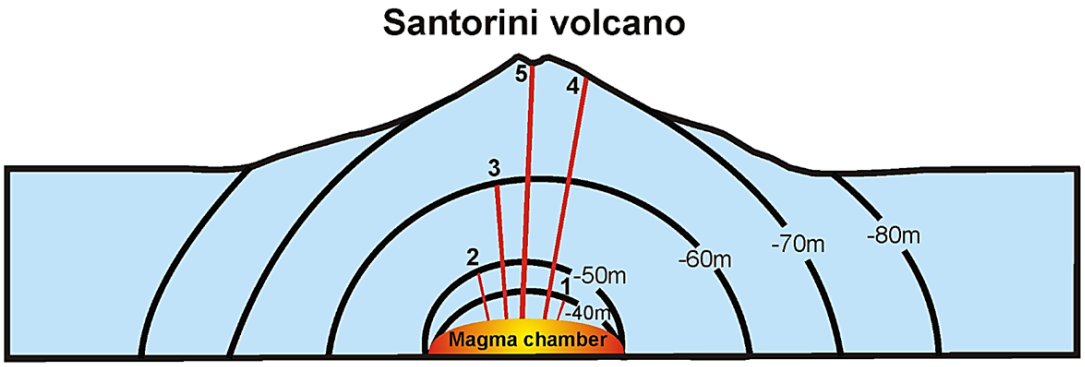

Fig. 44. Example of a gradual stress homogenisation that makes the stress field favourable for dike-fed eruptions (cf. Fig. 43). In this example, sea-level changes at Santorini Volcano, Greece, are the stress source. The sea-level changes correlate with glacial/interglacial periods so that the level falls (below the present interglacial/Holocene level) during glacial periods. As the sea-level falls, induced tensile stresses that gradually spread from the shallow magma chamber to the surface, thereby encouraging dike-fed eruptions. The gradual expansion of the favourable stress field for dike propagation is indicated by black semi-circular/semi-elliptical curves within which induced tensile stresses favour dike propagation for a given sea level fall. The red straight lines, numbered 1 to 5, indicate schematically the potential propagation paths of five dikes. More specifically, when the sea level has fallen to −40 m below its present level, the induced tensile stress is limited to a semi-elliptical zone close to the chamber (the outer boundary of the zone is the −40 m curve) and all injected dikes (here represented by dike 1) tend to become arrested (or change into sills). As the sea level falls further, tensile stress spreads through the roof of the chamber. At the level of −50 m and −60 m the outer boundaries of the induced high-tensile stress zones are still well below the surface, so the injected dikes (represented by dikes 2 and 3) tend to become arrested. As the sea level falls to −70 m and, particularly, −80 m, however, the induced tensile stresses reach the surface of the volcano, and dike-fed eruptions (represented by dykes 4 and 5) are encouraged (modified from Satow et al. 2021).

confined to the zones enclosed by contour 1 – and the seismic cycle begins again. Thus, active fault zones such as the SISZ, offer excellent examples of stress concentrations and associate gradients, that gradually become levelled out in the sense that the entire zone or area becomes subject to very similar stresses – generating stress homogenisation – that are then favourable for large fault slip, large earthquakes, and resulting (temporary for an active zone) in diminishing or disappearance of large-scale stress gradients.

Gradual stress transfer or migration away from the source so as to reduce of minimise the stress gradient and homogenise the stress field in a large volume can also be observed around some magma chambers. This is particularly so when the magma chamber is, in addition to any internal excess magmatic pressure, subject to external and gradually increasing loading. Such a situation is common for magma chambers at plate boundaries and may contribute to the formation of local sheet swarms and eventual eruptions (Fig. 43).

An excellent example of such gradual stress transfer – stress homogenisation and, thereby, gradient reduction – is provided by Santorini (Figs 32 and 33). Most eruptions on Santorini are supplied with magma through radial dikes and inclined sheets (Figs 28 and 32). The inferred shallow magma chamber at Santorini is at about 4 km depth (Fig. 33) and is subject to excess pressure from time to time when it receives magma from a deeper (but as yet undetermined) source. However, in addition to the internal excess pressure there has been

loading of the crustal segment hosting the chamber through sea-level changes (Satow et al., 2021). Most eruptions on Santorini in the past few hundred thousand years have occurred when the sea-level was much lower (during glacial periods) than today. Satow et al. (2021) show, through numerical modelling, that as the sea-level falls during ice periods, tensile stresses develop around the Santorini shallow magma chamber. More specifically, the tensile stress concentration around the chamber becomes noticeable when the sea level has fallen some 40 m below the current level.

As the sea level gradually falls further, to a maximum of about 80 m below the current level, the induced tensile stress spreads through the roof of the chamber and, eventually, reaches the surface of Santorini (Fig. 44). The concentration and subsequent spreading of the tensile stress due to sea-level fall encourages dike injection from the shallow magma chamber and eventually dike-fed eruptions. Thus, the correlation between eruption frequency at Santorini and low sea level is likely to be largely the result of concentration and then spreading of tensile stresses in the roof of the associated shallow magma chamber during falling sea level during the glacial (ice) periods. The stress gradients generated through the sea-level induced tensile stress concentration are subsequently diminished through the dike injections, which tend to bring the state of stress again closer to isotropic.

Summary and conclusions

Rock fractures are of fundamental importance in that they are the primary control of many of the earth's physical processes. These include volcanic eruptions, tectonic earthquakes, crustal-fluid transport, and plate-boundary formation and development. Rock fractures are of two main mechanical types: shear fractures and extension fractures. The former include all faults and some joints, while the latter include tectonic tension fractures as well all fluid-driven factures, including dikes, sills, and inclined sheets. While fracture formation is commonly attributed to stress concentrations, the mechanical effects of the fractures on the local stresses have received less attention. More specifically, how does rock-fracture formation of different types affect the local stresses within which they are generated? In particular, how does fracture formation and development affect local stress fields and stress gradients? Also, what is the 'ultimate' or stable stress local state of stress which all fracture formation, and brittle deformation in general, seeks to bring about?

This paper attempts to answer the questions raised above. The main findings and conclusions of the paper may be summarised as follows.

1. All tectonic rock fractures develop in response to local stresses. The local stresses are different from the stresses in the surrounding (host) rocks because the mechanical properties or the geometry (or both) of the region where the fractures develop are different from those in the surrounding parts of the crust. The stress magnitudes in the local areas of fracture development may be lower than those in the surrounding rocks, but more commonly they are higher, so that the stresses are raised or concentrated in the local region of fracture development.

2. When the local stresses vary in direction, that is, are anisotropic, so that the principal stresses are of different magnitudes, there will be a local stress gradient. The gradients can be very local – occurring within small rock bodies, such as pebbles in sedimentary rocks and pyroclasts of various sizes embedded in more fine-grained ash layers – or on an outcrop to a more regional scale, such as the scale of large regional dikes or large fault zones. In the present paper, the focus is on the latter, that is, stress gradients on an outcrop to kilometre scales.

3. While the basic stress conditions for rock-fracture formation, both extension fractures and shear fractures (faults), have received much attention and been the subject of detailed analyses over a long period of time, the overall effect of fracture formation, such as dike emplacement and fault slip, on associated stress gradients have received much less attention and little, if any, detailed mechanical analyses before the present work.

4. Here it is proposed that the main mechanical result of fracture formation and development is to minimise the stress difference that exist in the area of fracturing and, thereby, to reduce existing stress gradients. More specifically, fracture development brings the state of stress closer to that of isotropic, that is, lithostatic, and thereby diminishes any stress gradients within the rock body or regional of fracture formation and development.

5. Using dikes in Santorini (Greece) as examples of the effect of extension fracture formation on local stresses, it is shown that the overpressure (driving pressure) of a dike increases the (compressive) magnitude of the local minimum principal compressive stress σ_3 (as it was before dike injection) and brings it closer to the local maximum principal compressive stress σ_1 thereby making the state stress in the region surrounding the dike (its host rock), temporarily, close to isotropic (lithostatic). It follows that any stress gradients affecting regions with dimensions similar the dimensions of the dike will be reduced.

6. Using faults from Iceland as examples, it is shown that all faulting tends to bring the state of stress towards isotropic, thereby reducing any stress difference and stress gradients. In particular, normal faulting increases the (compressive) magnitude of pre-faulting σ_3 while somewhat reducing pre-faulting σ_1 at a given depth in the Earth's crust. By contrast, reverse (and thrust) faulting reduces the pre-faulting σ_1 and increasing somewhat at a given depth the pre-faulting σ_3. As for strike-slip faulting, it also reduces the pre-faulting σ_1 and increases the pre-faulting σ_3. Thus, all faulting tends to reduce the difference between the principal stresses, on a local and, for large fault-slip (but depending on the exact size of the slip surface), a regional scale. The overall effect of all faulting is thus to bring the local (or regional) state of stress closer to isotropic and to reduce the associated stress gradients.

7. In tectonically active areas, such as at plate boundaries, reduction in stress differences and stress gradients through tectonic fracture formation is always temporary. This is because the loading by the tectonic forces operating in active areas results in renewed stress concentrations and, thereby, renewed stress gradients. Eventually, however, as a given crustal segment drifts away from the sites of renewed tectonic activity, the final main phase of tectonic fracturing tends to bring the state of stress in the segment close to isotropic (lithostatic) and, thereby, permanently reduces its stress gradients.

Acknowledgements

Some of the results presented here derive from various projects on tectonic fracture formation and development, particularly in Santorini and Iceland. These projects have been funded by the Icelandic Science Foundation, the Research Council of Norway, the Volkswagen Foundation in Germany, the Natural Environmental Research Council of the United Kingdom, and the European Research Council.

References

Agustsdottir T, Woods J. et al. 2016. Strike-slip faulting during the 2014 Bardarbunga-Holuhraun dike intrusion, central Iceland. *Geophysical Research Letters*, **43**, 1495–503. doi: 10.1002/2015GL067423.

Andrew, R.E.B. & Gudmundsson, A. 2008. Volcanoes as elastic inclusions: their effects on the propagation of dykes, volcanic fissures, and volcanic zones in Iceland. *Journal of Volcanology and Geothermal Research*, **177**, 1045-1054.

Andrews, D.G. 2010. *An Introduction to Atmospheric Physics*, 2nd ed. Cambridge University Press, Cambridge.

Babiker, M. & Gudmundsson, A. 2004. Geometry, structure and emplacement of mafic dykes in the Red Sea Hills, Sudan. *Journal of African Earth Sciences*, **38**, 279-292.

Barton, C.A., Zoback, M.D & Moos, D. 1995. Fluid flow along potentially active faults in crystalline rock. *Geology*, **23**, 683-686.

Bazargan, M. & Gudmundsson, A. 2019. Dike-induced stresses and displacements in layered volcanic zones. *Journal of Volcanology and Geothermal Research*, **384**, 189-205.

Bazargan, M. & Gudmundsson, A. 2020. Stresses and displacements in layered rocks induced by inclined (cone) sheets. *Journal of Volcanology and Geothermal Research*, **401**, doi.org/10.1016/j.jvolgeores.2020.106965.

Bear, J. 1988. *Dynamics of Fluids in Porous Media*. Dover, New York.

Becerril, L., Galindo, I., Gudmundsson, A. & Morales, J.M. 2013. Depth of origin of magma in eruptions. *Scientific Reports*, **3**, 2762, doi.org/10.1038/srep02762.

Bergerat, F. 2021. Iceland, an emerging ocean rift. In: B. van Vliet-Lanoe (ed), *Iceland within the Northern Atlantic 1: Geodynamics and Tectonics.* Wiley, Hoboken (NJ), pp. 21-113.

Bergerat, F., Angelier, J. & Villemin, T. 1990 Fault systems and stress patterns on emerged oceanic ridges: a case study in Iceland. *Tectonophysics*, **179**, 183-197.

Bergerat, F., Gudmundsson, A., Angelier, J. & Rögnvaldsson, S.T. 1998 Seismotectonics of the central part of the South Iceland Seismic Zone. *Tectonophysics*, **298**, 319-335.

Bergerat, F., Angelier, J., Gudmundsson, A. & Torfason, H. 2003 Push-ups, fracture patterns, and palaeoseismology of the Leirubakki Fault, South Iceland. *Journal of Structural Geology*, **25**, 591-609.

Biswas, S.K., Saha, K., Das, G. & Mondal, T.K., 2023. Estimation of magma overpressure from partially exposed dykes – a new approach. *Journal of Structural Geology*, **168,** doi.org/10.1016/j.jsg.2023.104822.

Björnsson, A. 1985. Dynamics of crustal rifting in NE Iceland. *Journal of Geophysical Research*, **90**, 10,151-10,162.

Boresi, A.P. & Sidebottom, O.M. 1985. *Advanced Mechanics of Materials,* 4th ed. Wiley, New York.

Brebbia, C.A. & Dominquez, J. 1992. *Boundary Elements: an Introductory Course*. Computational Mechanics, Boston.

Browning, J., Drymoni, K. & Gudmundsson, A. 2015. Forecasting magma-chamber rupture at Santorini volcano, Greece. *Scientific Reports*, **5**, 15785, doi: 1038/srep15785.

Corti, N., Bonali, F.L. et al. 2023. Feeders vs arrested dikes: a case study from the Younger Stampar eruption in Iceland. *Journal of Volcanology and Geothermal Research*, **443**, doi.org/10.1016/j.jvolgeores.2023.107914

Deb, D. 2006. *Finite Element Method: Concepts and Applications in Geomechanics*. Phi Learning, New Delhi.

Desurvire, E. 2009. *Classical and Quantum Information Theory: An Introduction for the Telecom Scientist.* Cambridge University Press, Cambridge.

Druitt, T. H. Edwards, L. & Mellors, R. 1999. Santorini volcano. *Geological Society of London Memoir* **19**, pp. 1–165.

Drymoni K., Browning J. & Gudmundsson, A. 2020. Dyke-arrest scenarios in extensional regimes: insights from field observations and numerical models. Santorini Greece. *Journal of Volcanology and Geothermal Research*, **396**, 106854, doi.org/10.1016/j.jvolgeores.2020.106854

Drymoni, K., Browning J. & Gudmundsson, A. 2021. Volcanotectonic interactions between inclined sheets, dykes, and faults at the Santorini Volcano. Greece. *Journal of Volcanology and Geothermal Research*, **416,** 107294, doi.org/10.1016/j.jvolgeores.2021.107294.

Drymoni, K., Browning, J. & Gudmundsson, A. 2022. Spatial and temporal volcanotectonic evolution of Santorini volcano, Greece. *Bulletin of Volcanology*, **84**, 60, doi.org/10.1007/s00445-022-01566-4.

Durrant, A.V. 1996. *Vectors in Physics and Engineering*. Chapman & Hall, London.

Dzurisin, D. 2006. *Volcano deformation: new geodetic monitoring techniques*. Springer Verlag, Heidelberg.

Fyfe, W.S, Price, N.J. & Thompson, A.B. 1978. *Fluids in the Earth's Crust: Their Significance in Metamorphic, Tectonic and Chemical Transport Processes*. Elsevier, Amsterdam.

Galindo, I. & Gudmundsson, A. 2012. Basaltic feeder dykes in rift zones: geometry, emplacement, and effusion rates. *Natural Hazards and Earth System Sciences*, **12**, 3683-3700.

Geshi, N. & Neri, M. 2014. Dynamic feeder dyke systems in basaltic volcanoes: the exceptional example of the 1809 Etna eruption (Italy). *Frontiers in Earth Science*, **2**, doi: 10.3389/feart.2014.00013.

Geshi, N., Kusumoto, S. & Gudmundsson, A. 2012. Effects of mechanical layering of host rocks on dike growth and arrest. *Journal of Volcanology and Geothermal Research*, **223-224**, 74-82.

Gudmundsson, A. 1988. Effect of tensile stress concentration around magma chambers on intrusion and extrusion frequencies. *Journal of Volcanology and Geothermal Research*, **35**, 179-194.

Gudmundsson, 2006. How local stresses control magma-chamber ruptures, dyke injections, and eruptions in composite volcanoes. *Earth-Science Reviews*, **79**, 1-31.

Gudmundsson, A. 2011. *Rock Fractures in Geological Processes.* Cambridge University Press, Cambridge.

Gudmundsson, A. 2017. *The Glorious Geology of Iceland's Golden Circle.* Springer-Nature, Heidelberg.

Gudmundsson, A. 2020. *Volcanotectonics: Understanding the Structure, Deformation and Dynamics of Volcanoes.* Cambridge University Press, Cambridge.

Gudmundsson, A. 2022a. The propagation paths of fluid-driven fractures in layered and faulted rocks. *Geological Magazine*, **159**, 1978-2001, doi.org/10.1017/S0016756822000826

Gudmundsson, A. 2022b. Transport of geothermal fluids along dikes and fault zones. *Energies*, **15**, doi.org/10.3390/en15197106.

Gudmundsson, A., Bergerat, F. Angelier, J. & Villemin, T. 1992. Extensional tectonics of southwest Iceland. *Bulletin of the Geological Society of France*, **163**, 561-570.

Gudmundsson, A., Bergerat, F. & Angelier, J. 1996. Off-rift and rift-zone palaeostresses in Northwest Iceland. *Tectonophysics*, **255,** 211-228.

Gudmundsson, A. & Homberg, C. 1999. Evolution of stress fields and faulting in seismic zones. *Pure and Applied Geophysics*, **154**, 257-280.

Gudmundsson, A. & Brenner, S.L. 2005. On the conditions of sheet injections and eruptions in stratovolcanoes. *Bulletin of Volcanology*, **67**, 768-782.

Gudmundsson, A. & Andrew, R.E.B. 2007. Mechanical interaction between active volcanoes in Iceland. *Geophysical Research Letters*, **34**, L10310, doi:10.1029/2007GL029873.

Gudmundsson, A., Friese, N., Galindo, I. & Philipp, S.L. 2008. Dike-induced reverse faulting in a graben. *Geology*, **36**, 123-126.

Gudmundsson, A., Simmenes, T.H., Larsen, B., Philipp, S.L. 2010. Effects of internal structure and local stresses on fracture propagation, deflection, and arrest in fault zones. *Journal of Structural Geology*, **32**, 1643-1655.

Gudmundsson, A., Lecoeur, N., Mohajeri, N. & Thordarson, T. 2014. Dike emplacement at Bardarbunga, Iceland, induces unusual stress changes, caldera deformation, and earthquakes. *Bulletin of Volcanology*, **76,** doi: 10.1007/s00445-014-0869-8.

Gudmundsson, A. & Loetveit, I.F. 2005. Dyke emplacement in a layered and faulted rift zone. *Journal of Volcanology and Geothermal Research*, **144**, 311-327.

Gudmundsson, A. & Loetveit, I.F. 2012. Sills as fractured hydrocarbon reservoirs: examples and models. In: Spence, G. H., Redfern, J., Aguilera, R., Bevan, T. G., Cosgrove, J. W., Couples, G. D.& Daniel, J.-M. (eds). *Advances in the Study of Fractured Reservoirs*. Geological Society, London, Special Publications, **374**, doi.org/10.1144/SP374.

Jakobsdottir, S. 2008. Seismicity in Iceland: 1994-2007. *Jökull - The Icelandic Journal of Earth Sciences*, **58,** 75-100.

Jing, L. & Hudson, J.A., 2002. Numerical models in rock mechanics. *International Journal of Rock Mechanics and Mining Sciences*, **39**, 409-427.

Kusumoto, S., Geshi, N. & Gudmundsson, A. 2013. Aspect ratios and magma overpressure of non-feeder dikes observed in the Miyakejima volcano (Japan), and fracture toughness of its upper part. *Geophysical Research Letters*, **40**, 1065–1068, doi.org/10.1002/grl.50284.

Laurendeau, N.M. 2005. *Statistical Thermodynamics: Fundamentals and Applications.* Cambridge University Press, Cambridge.

Logan, D.L. 2016. *A First Course in the Finite Element Method*, 6th ed. Brooks/Cole, Pacific Grove (USA).

Marsden, J.E. & Tromba, A. 2012. *Vector Calculus*, 6th ed. W.H. Freeman, New York.

Masoud, A.A. 2020. Geometry and field relations disclose the emplacement dynamics of the SW Sinai dyke swarms (Egypt). *Journal of Volcanology and Geothermal Research*, **395**, 106831. https://doi.org/10.1016/j.jvolgeores.2020.106831.

Michel, J., Baumgartner, L. et al. 2008. Incremental growth of the Patagonian Torres del Paine laccolith over 90 k.y. *Geology*, **36**, 459-462.

Mohajeri, N., Hsu, S.-C., Milner, J., Taylor, J., Kieswetter, G., Gudmundsson, A., Kennard, H., Hamilton, I. & Davis, M., 2023. Urban–rural disparity in global estimation of PM2·5 household air pollution and its attributable health burden. *Lancet Planetary Health*, **7,** e660–72.

Perissoratis, C. 1995. The Santorini volcanic complex and its relation to the stratigraphy and structure of the Aegean arc, Greece. *Marine Geology*, **128**, 37-58.

Philipp, S.L., Afsar, F. & Gudmundsson, A. 2013. Effects of mechanical layering on hydrofracture emplacement and fluid transport in reservoirs. *Frontiers in Earth Science*, **1**, doi: 10.3389/feart.2013.00004.

Saemundsson, K. 2009. Geothermal systems in global perspective. 1-11, *Exploration for Geothermal Resources*, UNU-GTP, KenGen and GDC, Kenya, November 1-22, 2009.

Satow, C., Gudmundsson, A. et al. 2021. Eruptive activity of the Santorini Volcano controlled by sea-level rise and fall. *Nature Geoscience*, **14**, 586-592.

Savin, G.N. 1961. *Stress Concentration Around Holes*. Pergamon, New York.

Segall, P. 2010. *Earthquake and volcano deformation.* Princeton, Princeton University Press.

Sigmundsson, F., Hooper, A., et al. 2015. Segmented lateral dyke growth in a rifting event at Barðarbunga volcanic system, Iceland. *Nature*, **517**, 191-U158, doi:10.1038/nature14111.

Sneddon, I. N. & Lowengrub, M. 1969. *Crack Problems in the Classical Theory of Elasticity*. Wiley, London.

Sommerfeld, A., 1964. *Thermodynamics and Statistical Mechanics*. Academic Press, New York.

Sturge, M.D., 2003. *Statistical and Thermal Physics: Fundamentals and Applications*. CRC Press, Boca Raton.

Tibaldi, A., 2015. Structure of volcano plumbing systems: a review of multi-parametric effects. *Journal of Volcanology and Geothermal Research*, **298**, 85-135.

Townend, J. & Zoback, M.D. 2000. How faulting keeps the crust strong. *Geology*, **28**. 399-402.

Villemin, T., Bergerat, F. & Angelier, J. 1994. Brittle deformation and fracture patterns on oceanic rift shoulders: the Esja peninsula, SW Iceland. *Journal of Structural Geology*, **16**, 1641-1654.

Wells, N.C., 2011. The Atmosphere and Ocean: A Physical Introduction. 3rd ed. Wiley, London.